Volume 10
Number 16
21 August 2020
Pages 5309–5690

Catalysis Science & Technology

rsc.li/catalysis

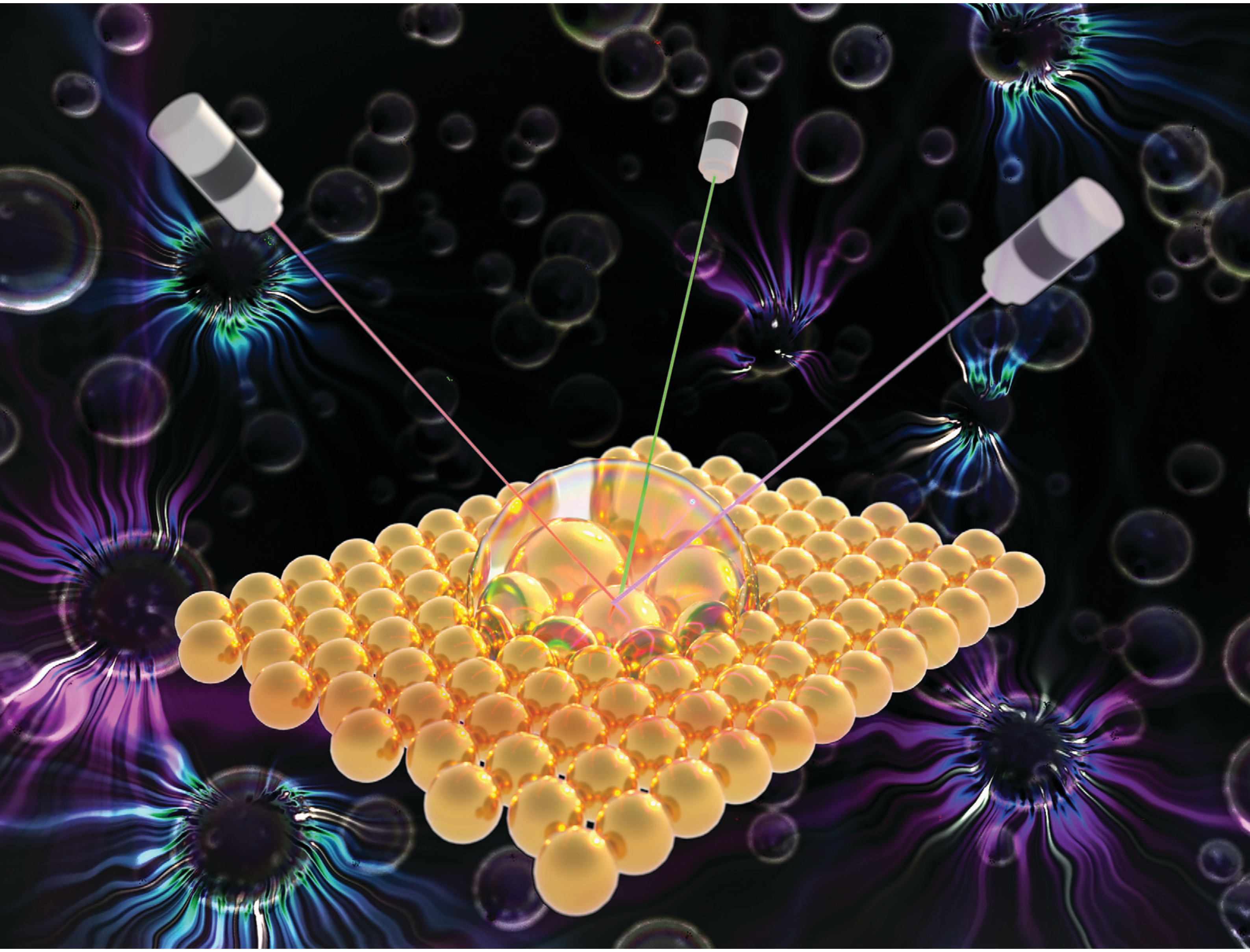

ISSN 2044-4761

ROYAL SOCIETY OF CHEMISTRY

MINIREVIEW
Leila Negahdar, Adam F. Lee *et al.*
Shining light on the solid–liquid interface: *in situ*/*operando* monitoring of surface catalysis

Catalysis
Science &
Technology

ROYAL SOCIETY
OF CHEMISTRY

MINI REVIEW

View Article Online
View Journal | View Issue

Check for updates

Cite this: *Catal. Sci. Technol.*, 2020, **10**, 5362

Received 19th March 2020,
Accepted 3rd June 2020

DOI: 10.1039/d0cy00555j

rsc.li/catalysis

Shining light on the solid–liquid interface: *in situ*/*operando* monitoring of surface catalysis

Leila Negahdar,*[ab] Christopher M. A. Parlett, [cde] Mark A. Isaacs, [ab] Andrew M. Beale, [ab] Karen Wilson [f] and Adam F. Lee *[f]

Many industrially important chemical transformations occur at the interface between a solid catalyst and liquid reactants, despite which relatively little attention has been paid to spectroscopic methods for interrogating the working solid–liquid interface. This partly reflects a limited number of analytical techniques that give access to interface-specific information. Direct observation of surface species at catalytic solid–liquid interfaces is a daunting challenge for many *in situ* techniques due to the low concentration and/or short lifetime of chemical species in dynamic reactions. This review discusses the application of *in situ* and *operando* spectroscopies to probe solid–liquid interfaces, with a focus on the resulting mechanistic insight in the context of catalysis for sustainable chemistry.

1. Introduction

The rational design of heterogeneous catalysts with optimal performance heavily relies on a detailed understanding of atomic and molecular interactions and associated reactions at solid surfaces, for which *in situ* (in place) and *operando* (under working conditions) studies can offer unparalleled insight.[1–3] Heterogeneous catalysis, wherein the reactants and catalyst are in different phases, occurs at solid–gas, solid–liquid, or solid–liquid–gas interfaces[4] (and exceptionally at the liquid–gas interface[5]) and involves a complex interdependency between adsorption/desorption, diffusion, and speciation processes, which dictate reaction kinetics and mechanisms.[6] Heterogeneous catalysis underpins chemicals, pharmaceuticals, and fuels production from fossil and biomass resources.[7,8]

Numerous industrial catalytic processes are conducted in the liquid phase, however the number of *in situ* and/or *operando* studies of catalytic transformations at the solid–liquid interface are limited, in part due to the lack of techniques able to provide quantitative and chemically specific information on such interfaces. Over the past decade, infrared, Raman, UV-vis and X-ray spectroscopies have been extended to elucidate the nature of active sites in reacting catalyst surfaces (*e.g.* their phase, oxidation state and density) and molecular processes such as adsorption of reactants and products (strength and geometry) and the identification of reactive surface intermediates. This review highlights the emerging mechanistic insight available through applying *in situ*/*operando* spectroscopies to catalytic reactions at the solid–liquid interfaces, and identifies creative solutions to current challenges in liquid phase heterogeneous catalysis. Popular spectroscopic techniques and state-of-the-art methodologies, and their advantages and limitations are critically discussed for exemplar systems, particularly in the context of sustainable chemistry. Requisite conditions for reaction analysis, and the types of information that can be determined, notably reaction mechanisms and catalytically active species, are outlined. Concluding remarks address the current status and future perspectives for emerging spectroscopic techniques as applied to liquid phase heterogeneous catalysis.

2. Spectroscopic techniques

In situ catalytic studies at the solid–liquid interface are extremely challenging.[9] First, the reaction medium plays a significantly greater role than occurs in solid–gas catalysis. The high density of liquids results in increased absorption of incident and transmitted/radiated photons, and greater scattering/attenuation of photoexcited electrons in electronic spectroscopies, and hence poorer signal:noise in resulting spectra. Where water is the solvent of choice, such as for water-splitting to H_2, such issues are particularly problematic

---

[a] *Department of Chemistry, UCL, 20 Gordon Street, London, WC1H 0AJ, UK. E-mail: l.negahdar@ucl.ac.uk*
[b] *UK Catalysis Hub, Research Complex at Harwell, Rutherford Appleton Laboratory, Harwell, Oxfordshire, OX11 0FA, UK*
[c] *Department of Chemical Engineering & Analytical Science, The University of Manchester, Manchester, M13 9PL, UK*
[d] *Diamond Light Source, Harwell Science and Innovation Campus, Didcot, Oxfordshire, OX11 0DE, UK*
[e] *Diamond Light Source, University of Manchester at Harwell, Harwell Science and Innovation Campus, Didcot, Oxfordshire, OX11 0DE, UK*
[f] *Centre for Advanced Materials and Industrial Chemistry (CAMIC), School of Science, RMIT University, Melbourne, VIC3000, Australia. E-mail: adam.lee2@rmit.edu.au*

when using IR spectroscopy. Second, a multitude of species may co-exist at solid–liquid interfaces, including reactants, intermediates, spectators, products and solvents, some of which may occur at concentrations high enough to obscure signals from other species. Third, the dynamic nature of solid–liquid interfaces arising from exchange between the bulk media and local environment can induce broadening of spectral features. For example, at 0 °C, the vapour pressure of water is associated with the exchange of around three million monolayers per second of molecules between a liquid surface and vapour phase.[10] Finally, under most experimental conditions a solvent is contacted by other phases (such as vapour/gas) or insoluble/immiscible reactants and products which can alter the density of liquid at the solid surface.[11–13] Common *in situ*/*operando* spectroscopies applied to catalysis at the solid–liquid interface are summarised below.

2.1 Attenuated total reflection infrared spectroscopy (ATR-IR)

The vibrational spectrum of a molecule adsorbed on a solid surface includes information about the surface–adsorbate bonds, the intermolecular interactions and the local orientation of the molecule. Such detailed information makes vibrational spectroscopy, especially in the infrared (IR), a valuable technique in the field of heterogeneous catalysis. IR spectroscopy has been extensively applied to catalytic solid–gas interfaces. However, studies of liquid phase catalysis by IR spectroscopy are more limited due to large spectral interference from the liquid phase. Much of the experimental IR spectroscopic data available on solid–liquid catalyst interfaces has been obtained using attenuated total reflection infrared spectroscopy (ATR-IR).[14] ATR-IR spectroscopy is suitable for studying molecular vibrations at the solid–liquid interface because the IR light is restricted to the surface vicinity which minimises spectral contributions from the bulk liquid. Using ATR-IR, spectra are obtained from the absorption of light penetrating only a few microns orthogonal to the direction of travel through an optically transparent crystal, the internal reflection element (IRE) (Fig. 1), into a catalyst film. A multiple-bounce IRE increases the intensity of such evanescent IR light reaching the sample, and hence improves the signal to noise ratio, important for samples exhibiting low absorbances, such as heterogeneous catalysts containing a small number of surface sites.[12] ATR-IR spectra of a heterogeneous catalyst in the liquid phase can provide information on both soluble and adsorbed reactants, products and reactive intermediates. The detailed background and theory of ATR-IR spectroscopy has been recently reviewed.[4,6,14]

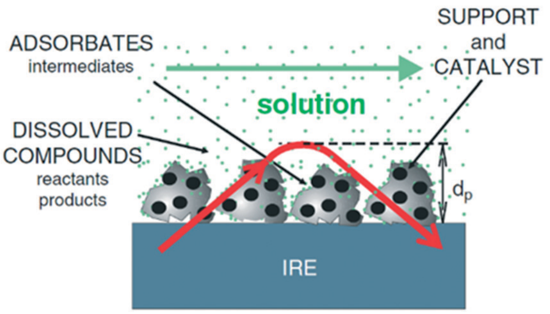

Fig. 1 Schematic of ATR-IR spectroscopy at the solid–liquid interface; the red arrow is the evanescent light propagating through the crystal and catalyst film, reproduced from ref. 14 with permission from Elsevier, copyright 2006.

2.1.1 Applications and limitations. ATR-IR spectroscopy has been applied to many heterogeneous catalytic systems include wastewater treatment, biomass conversion, electrochemistry and photocatalysis.[12,15] ATR-IR spectroscopy can provide useful information on the mechanism of wastewater remediation of contaminants such as nitrate/nitrite and bromate by catalytic hydrogenation, and on the transformation of many biomass-derived oxygenates. The technique can provide online monitoring of reactions by analysis of reactant/products in either the bulk fluid phase or at a catalyst surface. Such information is especially useful for kinetic studies at elevated temperatures and pressures within a reactor: an important advantage of ATR-IR spectroscopy is its potential for use in *operando*, especially in combination with other analytical methods. For example, small quantities of reaction products that cannot be detected by conventional analytical tools probing the bulk phase are often observable in ATR-IR spectra. Another advantage of ATR-IR spectroscopy is its sensitivity to changes in the state of metal catalysts due to their strong IR absorption, which can provide useful diagnostics.[14]

Moreover, ATR-IR spectroscopy can probe the volume of sample very close to the IRE, and hence is valuable for investigating powder catalysts coatings. However, the catalyst particle size, packing and the coating thickness influences the relative signals from the catalyst surface and bulk media.[16] Despite these complexities, ATR-IR spectroscopy can offer unique insight into competing catalytic reaction pathways.[17]

ATR-IR spectroscopy at the solid–liquid interface can however be challenging due to differences in the sensitivity of IR absorbing species and complexity of some reaction networks. Spectra collected at the solid–liquid interface comprise signals from both soluble and adsorbed species, including reactants, reaction intermediates, products and spectators. This array of species and resulting spectral complexity may necessitate additional experimental and/or computational investigations to discriminate between different species.[4] Low conversions, arising from limitations in the thickness of catalyst films that can be uniformly deposited on IRE crystals, may also necessitate additional analytic strategies, such as modulation excitation spectroscopy in conjunction with phase-sensitive detection, to decouple weak periodically varying reaction signals from large static ones associated with the bulk media or catalytic spectators.[18] Where multi-bounce IRE crystals are employed, varying concentration gradients can arise across the catalyst

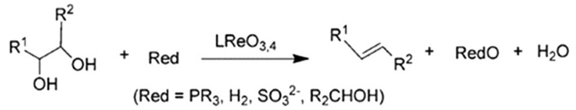

Scheme 1 Reduction of glycols to olefins, reproduced from ref. 23 with permission from Wiley-VCH, copyright 2013.

coatings, resulting in inconsistent surface chemistry and complicating analysis of the (spatially averaged) spectra. Changes in the reflectivity of liquids due to dissolved gas (*e.g.* H_2, N_2 or O_2) and/or catalysts due to surface oxidation or reduction present additional challenges to spectral interpretation.[4,14] The limit of detection of ATR-IR extends from a single monolayer (typically 10–20 Å of a surfactant or polymer, or a few tens of nanograms).[19,20] Surface sensitivity is relatively poor since penetration depths into the coated catalyst and/or bulk media are on the order of the wavelength (up to a few microns). However, depth profiling is possible if the sample is suitably prepared and spectral parameters carefully chosen.[21] Selected examples of successful applications of *operando* ATR-IR spectroscopy, and resulting mechanistic insight, are described in the following section.

2.1.2 Solid-acid-catalysed hydrolysis of cellulose in water. Weckhuysen *et al.* demonstrated the use of an autoclave reactor equipped with an ATR-IR spectroscopic probe as a useful tool for *in situ* monitoring of the solid acid catalysed hydrolysis of cellulose in water.[22] In combination with HPLC, time-resolved ATR-IR spectroscopy provided a detailed picture of the reaction mechanism. Cellulose hydrolysis proceeds *via* cleavage of the glycosidic linkages of cellulose, to form smaller cellulose units observable from C–O vibrational stretches at 1105 cm^{-1} in ATR-IR spectra. Over time, disaccharide units further hydrolysed into glucose, evidenced by 1075 and 1038 cm^{-1} vibrations (Fig. 2), which subsequently reacted to form 5-hydroxyfurfural (HMF) *via* isomerisation to fructose and eventual dehydration. The formation and accumulation of HMF was indicated by C=C vibrations at 1582 cm^{-1}, concomitant with the formation of formic acid, acetic acid and levulinic acid with C–O vibrations at around 1213, 1280, and 1172 cm^{-1} respectively. A vibration assigned to an aldehyde C=O stretch was also observed at 1664 cm^{-1}.

2.1.3 Reductive valorisation of bio-based feedstocks. The high oxygen content of biomass derived feedstocks such as carbohydrates and triglycerides require their hydrodeoxygenation for applications as high-value chemicals and fuels. For example, deoxydehydration (DODH) of bio-derived vicinal diols to alkenes, *via* reductive water elimination, has received increasing attention in recent years. Jentoft *et al.* studied the catalytic DODH of glycols over carbon supported perrhenate (ReO_x–C) (Scheme 1).[23] The kinetics of diethyl tartrate DODH were monitored by ATR-IR spectroscopy within a bespoke autoclave incorporating the IRE into the reactor side-wall (Fig. 3). Vibrational bands at 1731, 1295, 1155 and 979 cm^{-1} were assigned to diethyl fumarate, the only reaction product, whose rate of formation was inversely proportional to that of tartrate conversion (Fig. 4); calibration of IR band intensities enabled quantification of reactant and product concentrations. Detailed kinetic analysis suggested that the first polyol-to-olefin DODH reactions could be catalysed by immobilised (and at high temperature soluble) rhenium species using H_2 or hydrogen-transfer agents such as tetralin and benzyl alcohol. This ATR-IR reactor configuration, in which the catalyst is fluid, offered high sensitivity to liquid phase species, but was relatively insensitive to surface reaction intermediates.

2.1.4 Aqueous phase reforming and water-gas shift reaction of bio-based feedstocks. Immobilising a thin catalyst film on an IRE crystal and then passing a reaction solution over this is a common approach to *operando* studies of working catalyst surfaces. Catalyst film stability is critical, requiring careful control over the reactant flow rate to avoid disruption and loss from the ATR-IR set-up, but when successful obviates the need for IR transmission through the

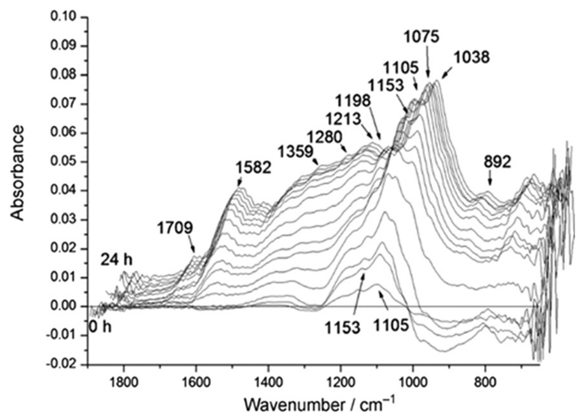

Fig. 2 Time-resolved differential ATR-IR spectra during solid acid catalysed hydrolysis of cellulose in water, reproduced from ref. 22 with permission from Wiley-VCH, copyright 2012.

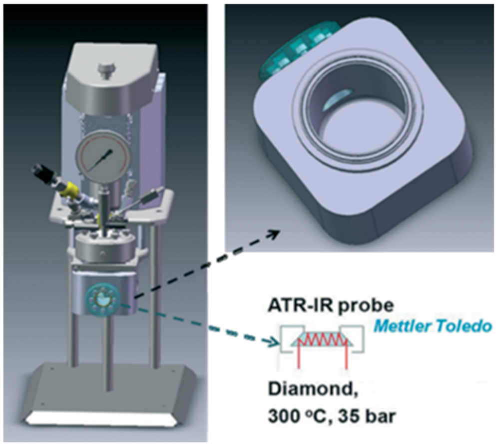

Fig. 3 Stirred batch reactor incorporating ATR-IR probe for *in situ* spectroscopy of liquid phase catalytic reductions, reproduced from ref. 23 with permission from Wiley-VCH, copyright 2013.

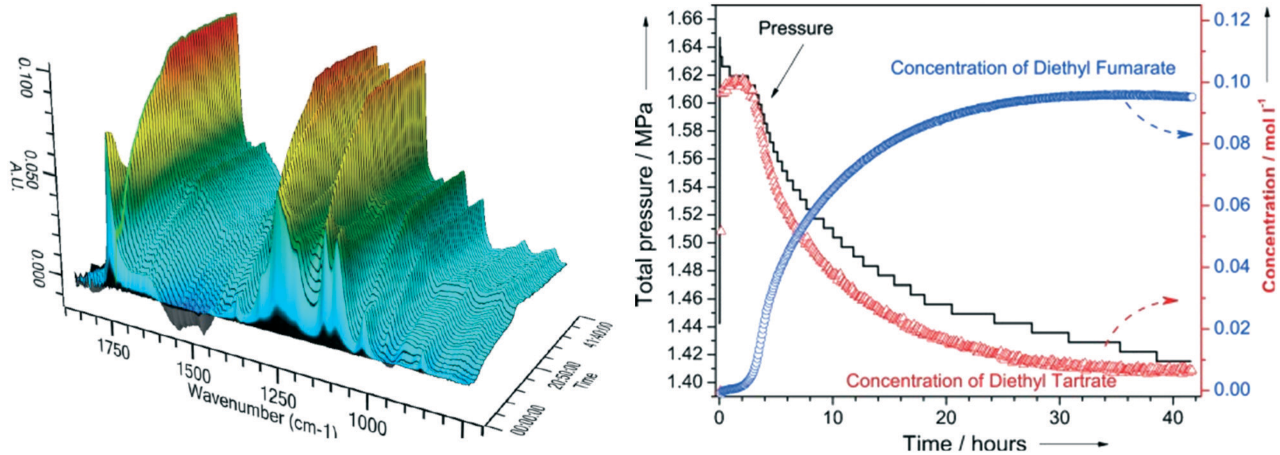

Fig. 4 (left) *In situ* ATR-IR spectra during DODH of diethyl tartrate over ReO_x–C at 150 °C; (right) corresponding reactant and product reaction profiles and H_2 pressure, reproduced from ref. 23 with permission from Wiley-VCH, copyright 2013.

bulk reaction medium.[16] Lercher *et al.* studied the aqueous phase reforming (APR) of glycerol, at relatively low temperature and elevated pressure, to elucidate the role of C–C and C–O bond cleavage during polyol conversion over supported Pt nanoparticles.[24] Spectra were collected using a trapezoidal ZnSe IRE within a stainless-steel continuous flow reactor placed inside an FTIR spectrometer (Fig. 5) as a function of temperature and reactant feed. A band at 1720 cm^{-1} indicated the formation of keto or aldehyde carbonyl groups; broad bands at 2050 and 1940 cm^{-1} were associated with linear and bridge bound CO on Pt >433 K. Asymmetric and symmetric stretching vibrations of surface carboxylates of ethanol and propanol on alumina were also observed at 1510 and 1434 cm^{-1} (Fig. 5). Spectroscopic and kinetic analysis (from a separate plug-flow reactor) revealed that dehydrogenation of hydroxyl groups at primary carbon atoms was followed by decarbonylation and subsequent water gas shift, or disproportionation to the acid and subsequent decarboxylation. Hydrogenolysis of C–O and C–C bonds was not observed.[24]

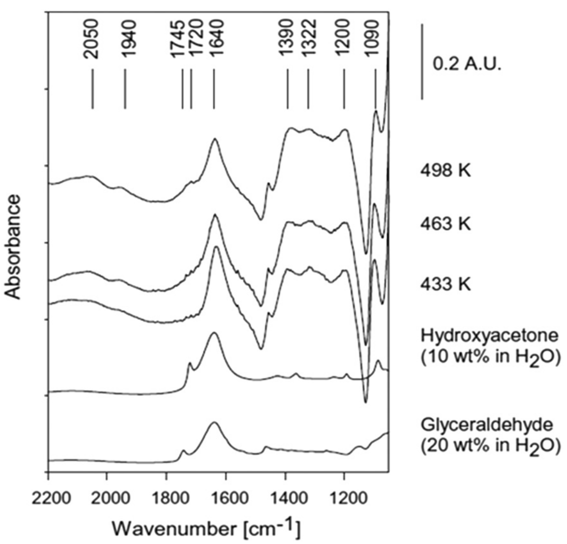

Fig. 5 ATR-IR spectra during reforming of 20 wt% glycerol on 3 wt% Pt/Al_2O_3, reproduced from ref. 24 with permission from Elsevier, copyright 2013.

Operando ATR-IR spectroscopy was also employed to study methanol reforming over Pt/Al_2O_3 at 423 K in the vapour (1.36 or 3.08 bar) or liquid (5.84 bar) phases.[25] Spectra were recorded using a horizontal flow cell, wherein the catalyst-coated ATR crystal was sealed by a Viton O-ring to a Teflon-coated aluminum frame. Different methanol partial pressures resulted in significant differences in adsorbed CO. The surface coverage of CO increased by 35% when switching from liquid to vapour reaction conditions, suggesting that methanol decomposition is more kinetically limiting in the liquid than vapour phase reaction. ATR-IR also implicated hydrogen co-adsorbed with CO on the Pt surface, evidenced by a shift in the linearly bound CO band. The same reactor configuration and catalyst was investigated for water–gas shift (WGS) to understand the effects of CO, H_2 and H_2O partial pressures in the vapour or liquid phase on the reaction mechanism.[25] In the vapour, Pt surfaces are covered by adsorbed CO, and hence reactions were zero order in CO pressure. A negative order was observed with respect to H_2 due to surface saturation by H adatoms. A fractional positive order with respect to water pressure confirmed the non-equilibrated dissociation of H_2O over Pt. Liquid phase studies revealed a slight decrease in the CO coverage for the same CO partial pressure, however the catalytic performance for the WGS reaction was comparable under liquid and vapour phase conditions. Pt/Al_2O_3 catalysed APR of ethylene glycol was similarly studied in a continuous flow, fixed bed reactor (Fig. 6) over a ZnSe IRE spray-coated with catalyst and placed inside a tunnel cell connected to a gas manifold.[26] The alumina support is unstable under most APR conditions, phase transitioning to boehmite. This transition occurred under more mild conditions than expected, resulting in irreversible catalyst deactivation. The resulting alumina restructuring escalated the rate of formation of hydrogen per

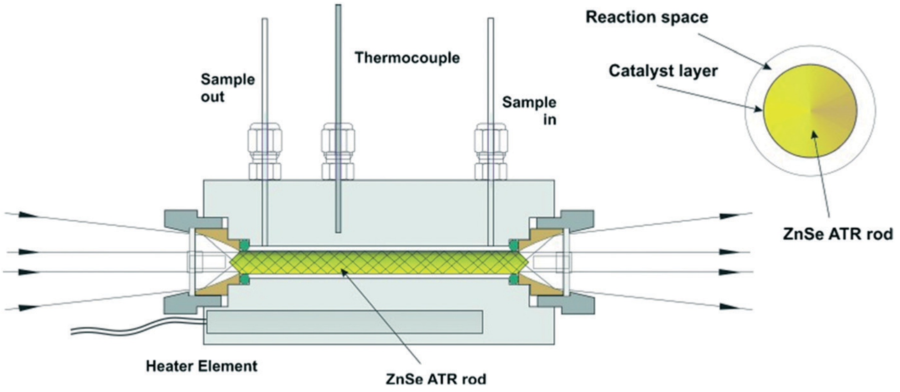

Fig. 6 ATR-IR tunnel cell and cross-section of the catalyst coated ZnSe IRE rod, reproduced from ref. 26 with permission from Wiley-VCH, copyright 2013.

surface Pt atom, with the enhancement correlating with the increase in concentration of surface OH groups and enhanced oxidation of Pt.

Pretreatment of catalyst films deposited on IRE crystals is critical to the success of liquid phase *in situ*/*operando* ATR-IR studies.[27] Such pretreatments typically comprise two steps: (i) flowing only the solvent (*i.e.* without dissolved reactants) for up to several hours to ensure mechanical stability of the catalyst film and the removal of any weakly bound adsorbates; and if required (ii) addition of dissolved H_2 or O_2 to the solvent stream to respectively remove oxidised or carbonaceous surface residues.[13,28,29] Copeland *et al.* studied the effect of pretreatment on Pt/γ-Al_2O_3 catalysts for glycerol APR,[27] identifying alternating flows of H_2 and O_2 saturated water as the most effective cleaning protocol. Subsequent ATR-IR spectroscopy showed that Pt/γ-Al_2O_3 activates glycerol at room temperature in water to form adsorbed CO. Optimal rates of CO formation correlated with the concentration of available surface Pt sites, some of which exhibited unique high reactivity. The highly reactive Pt sites preferentially adsorbed hydrogen and bridge-bound CO from glycerol reforming and directed the removal of bridging CO species *via* the water–gas shift reaction.

2.1.5 Alcohol oxidation. Benzyl alcohol oxidation has been studied over Pd/Al_2O_3 and Bi–Pd/Al_2O_3 in the liquid phase[15,30] using batch and continuous flow reactors to understand the molecular mechanism of the reaction; the continuous flow configuration enabling evaluation of different reaction conditions and determination of the intrinsic catalyst kinetics through varying film thickness on an IRE. ATR-IR measurements revealed three distinct reactions during benzyl alcohol oxidation (Scheme 2): alcohol dehydrogenation affording adsorbed hydrogen (reaction a); decarbonylation of the aldehyde product to adsorbed CO and benzene (reaction b); and benzaldehyde oxidation to benzoic acid, which was presumed to adsorb onto the Al_2O_3 support as benzoate. Atomic hydrogen liberated in step a is oxidised to water (reaction c) thereby regenerating the active site, with Pd overoxidation by excess O_2 (reaction d) proposed to induce catalyst deactivation although ATR-IR cannot directly

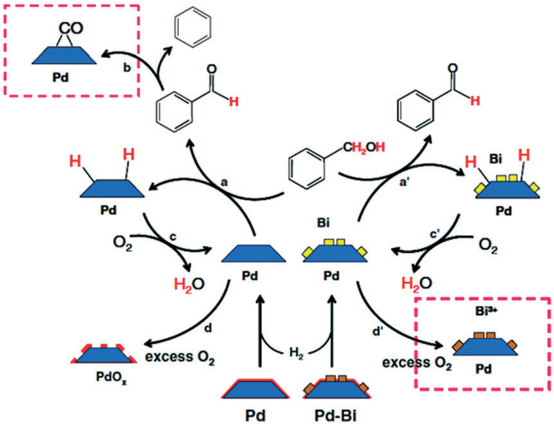

Scheme 2 Proposed mechanism of benzyl alcohol oxidation evinced by ATR-IR spectroscopy, reproduced from ref. 15 with permission from Springer Nature, copyright 2009.

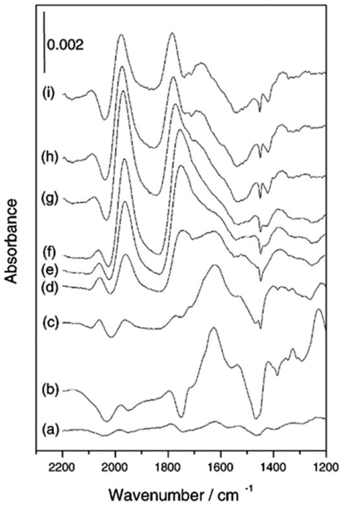

Fig. 7 (a)–(h) *In situ* ATR-IR spectra of Pt/Al_2O_3 in cyclohexane during CO_2/H_2 adsorption at 40 °C and (i) following exposure to N_2-saturated cyclohexane, reproduced from ref. 31 with permission from the Royal Society of Chemistry, copyright 2002.

measure metal oxidation. The latter proposal and role of Pd oxidation during alcohol oxidation has been hotly debated and will be addressed later. Analogous studies of Pd–Bi/Al_2O_3 revealed that Bi promotes oxidation by suppressing aldehyde decarbonylation (reaction b), concluded from the absence of surface bound CO vibrations, increasing overall selectivity and preventing catalyst poisoning.

2.1.6 CO_2 hydrogenation and CO adsorption/oxidation. CO_2 hydrogenation in cyclohexane was explored over a model Pt/Al_2O_3 catalyst deposited on an IRE and mounted within a bespoke, temperature-regulated flow cell.[31] A band at 1676 cm^{-1} (Fig. 7) was assigned to a carbonate-like species remote from the metal–support interface, whereas bands at 1628, 1326 and 1230 cm^{-1} were attributed to carbonate-like species adsorbed at the metal–support interface, which react to form CO.[31]

CO_2 was proposed to adsorb on Al_2O_3, to form carbonate-like species, which subsequently react with either dissociatively adsorbed H_2 over Pt (Fig. 8a) or an oxygen defect (Fig. 8b) to form CO at the metal–oxide interface; reactively-formed CO was thus inferred as a selective probe of such interfacial sites.

A valuable approach to detailed insight into supported noble metal catalysts is achieved *via* investigations of small and simple molecule conversion, such as CO. Lefferts *et al.* investigated the CO adsorption and oxidation on noble metal catalysts such as Pt/Al_2O_3 and Pd/Al_2O_3 with ATR-IR in both the gas and liquid phase.[28] Parameters such as the effect of water on adsorbed CO and the effect of pH on CO adsorption and oxidation were studied. Water and pH impart significant effects on the adsorption and oxidation of CO over Pt/Al_2O_3 and Pd/Al_2O_3. Furthermore, water also affected the metal particle potential and the adsorbed CO molecule, resulting in higher oxidation rates when conducted in liquid water compared to gas-phase conditions. pH also influenced the metal particle potential which in turn effected the observed oxidation rates.

2.1.7 Electrocatalytic conversion of formic acid to carbon monoxide over Pd catalyst. Surface-enhanced IR absorption spectroscopy (ATR-SEIRAS) has been applied in electrochemical cells. The mechanism of formic acid (FA) decomposition over Pd surfaces was investigated by SEIRAS[32] to elucidate the fate of CO_{ad} surface intermediate potentially formed at the Pd electrode, and whether its formation arises from a dehydration pathway. Complementary experiments were undertaken in a regular-volume ATR cell (Fig. 9A) and a thin-layer ATR flow cell (Fig. 9B) to determine whether for CO_{ad} is formed by direct dehydration of formic acid or reduction of the CO_2 dehydrogenation product. Integrated IR band intensities associated with formic acid, CO_2 and CO_{ad} were monitored during the reaction (Fig. 9). The CO_{ad} band was inversely related to the interfacial CO_2 concentration, suggesting that CO_{ad} mainly arose from reduction of the (FA) hydrogenation product CO_2 at potentials where adsorbed H species exist on Pd surfaces (Scheme 3).[32] This *in situ* mechanistic study may inform the development of new Pd based catalysts for hydrogen energy utilisation.

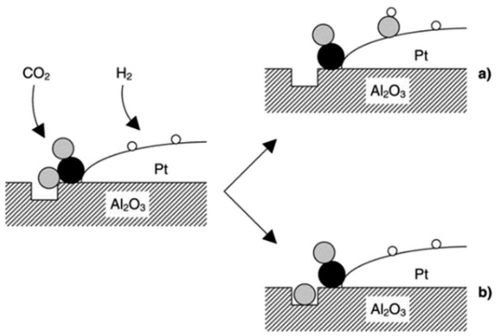

Fig. 8 Schematic of CO_2 reduction over a Pt/Al_2O_3 model catalyst by the reaction of an oxygen atom with either (a) adsorbed hydrogen to form a surface hydroxyl, or (b) a defect in the oxide surface. Black, grey and white balls depict carbon, oxygen and hydrogen atoms, respectively, reproduced from ref. 31 with permission from the Royal Society of Chemistry, copyright 2002.

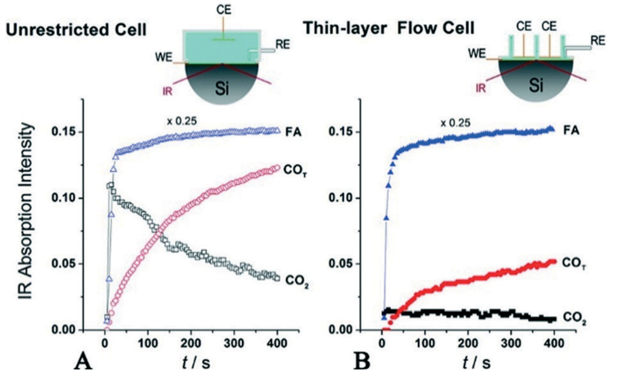

Fig. 9 Evolution of IR bands associated with near-surface CO_2 product, interfacial FA molecules in the solution phase and reactively-formed adsorbed CO_T species on the Pd surface. In (A), FA was added to the regular unrestricted ATR cell a fixed amount of $HClO_4$ electrolyte. In (B), FA-containing solution was pumped into the flow cell to replace the supporting base electrolyte, reproduced from ref. 32 with permission from the American Chemical Society, copyright 2011.

This *in situ* mechanistic study may inform the development of new Pd based catalysts for hydrogen energy utilisation.

2.1.8 ATR-IR microreactor design for kinetic studies. Careful integration of ATR-IR spectroscopy into reaction cells is critical if quantitative correlations between the concentrations of surface species and reaction kinetics are to be deduced and require that mass transport within such cells

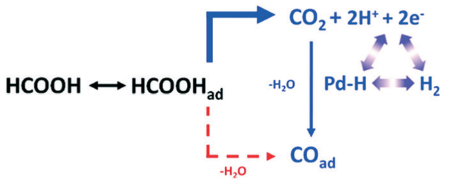

Scheme 3 Proposed reaction pathway from HCOOH to CO_{ad} over a Pd electrode *via* CO_2 as a reactive intermediate, reproduced from ref. 32 with permission from the American Chemical Society, copyright 2011.

is comparable with that of conventional catalytic microreactors. Unfortunately, the design of such spectroscopic cells often necessitates a compromise to accommodate the IRE crystal and catalyst film, resulting in only qualitative correlations. Diffusion from the bulk media to active sites, adsorption, desorption and diffusion back into the bulk media should all occur faster than the surface catalytic step to obtain the intrinsic reaction kinetics. A flow-through ATR-IR cell should possess the following criteria: (i) the cell volume must be small enough to allow rapid exchange of reactants/products without significant dead volumes; and (ii) the fluid velocity and concentration profiles entering the cell must be constant to simplify data analysis.[33]

Collins *et al.* constructed an ATR-IR microreactor cell using CO chemisorption over a thin platinum film to validate the design.[33] The cell comprised a jacketed liquid top plate for temperature control, and inlet and outlet ports to feed reagents and collect the resulting product stream. The IRE was fitted into the cell body, incorporating mirrors to focus the IR beam to/from the IRE crystal; these components were sealed by a Viton O-ring, and the resulting cavity between the body and top determined by the O-ring dimensions (Fig. 10 left).

2.2 Raman spectroscopy

The high sensitivity of IR spectroscopy to changes in dipole moment result in a strong signal from water, in contrast to Raman spectroscopy. This difference favours the use of Raman spectroscopy for *in situ*/*operando* studies of aqueous phase catalysis.[34,35] Conventional Raman, UV Raman and surface/tip-enhanced Raman spectroscopies (SERS and TERS) have been widely used to study heterogeneously catalysed reactions as illustrated in the following case studies.

2.2.1 Applications and limitations. The ability of Raman spectroscopy to provide detailed molecular information, under diverse environments, has resulted in its exploitation for numerous applications in heterogeneous catalysis. However, temperature effects require consideration when collecting Raman spectra at extreme reaction temperatures, notably the thermal stability of lenses used to collect scattered Raman light from hot catalysts. *In situ* Raman studies >150 °C are also hindered by sample emission in the IR region.[35] Elevated pressure measurements are feasible provided that the Raman reaction cell is appropriately designed. Conventional Raman spectroscopy is often hindered by fluorescence interference, although this can be overcome by changing the excitation source to the UV region (UV Raman),[36] a solution in itself problematic if photochemistry is initiated under higher energy UV irradiation. Undesired photochemistry can be suppressed by using reduced power laser sources, rotating/moving the catalyst, rastering the laser over the sample, or even fluidising catalyst particles.[37] The enormous signal enhancements available through SERS enable surface-selective detection down to the single molecule level, although the SERS-active nanostructure must be in close proximity or direct contact with the catalyst of interest which can introduce artefacts into the observed reactivity.[38] For example, energy transfer during SERS monitoring of Pt electrocatalysts can alter measured activity. SERS substrates must also exhibit good chemical and thermal stability under reaction conditions, and are typically restricted to Au, Ag, and Cu due to their strong SERS response.[38] TERS also suffers practical limitations associated with the very small size of tips which usually require sophisticated engineering. The chemical reactivity, short lifetime and instability of TERS probes in the liquid phase remain challenges to the broader application of the technique. Since Raman is a light scattering technique spectra can be collected from a very small catalyst volume (<1 μm diameter and <10 μm depth), with SERS and TERS variants sensitive to only a few monolayers of adsorbates.[19,39]

2.2.2 UV-Raman. Raman spectroscopy is a powerful technique for catalyst characterisation, however, fluorescence caused by impurities, organic species and defect sites, which usually occurs in the 300 to >700 nm range, can interfere with vibrational bands.[40] This interference can be avoided by using a UV excitation source (Fig. 11a).[37] Another advantage of UV Raman is its

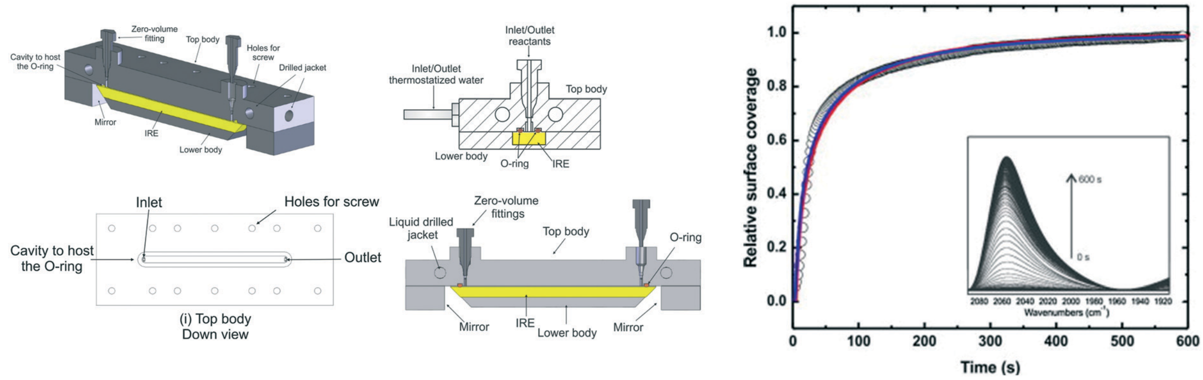

Fig. 10 (left) Schematic of ATR flow cell, and (right) time-dependent normalised IR signal of Pt–CO band at 2048 cm^{-1}. Lines are best fits to the data assuming a convection-diffusion model, reproduced from ref. 33 with permission from Elsevier, copyright 2014.

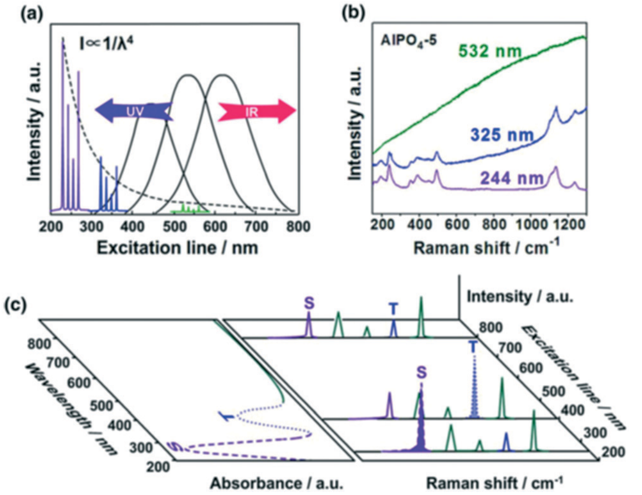

Fig. 11 a) UV Raman spectroscopy avoiding fluorescence interference while increasing Raman scattering intensity; b) Raman spectra of $AlPO_4$-5 excited at 532, 325, and 244 nm; c) a schematic description of UV resonance Raman spectroscopy, the Raman bands attributed to S and T components can be selectively enhanced by shifting the excitation laser lines towards their UV-visible absorption bands, reproduced from ref. 37 with permission from Springer Nature, copyright 2014.

sensitivity to surface vibrations, which is considerably higher than that of visible or near-IR Raman spectroscopy. Raman spectra of $AlPO_4$-5 excited by 532, 325, and 244 nm radiation illustrate the sensitivity enhancements achievable using short wavelength radiation (Fig. 11b).

Since electronic transitions of chemical compounds are also usually excited by UV irradiation, resonance Raman effects can enhance spectral quality by several orders of magnitude (Fig. 11c).

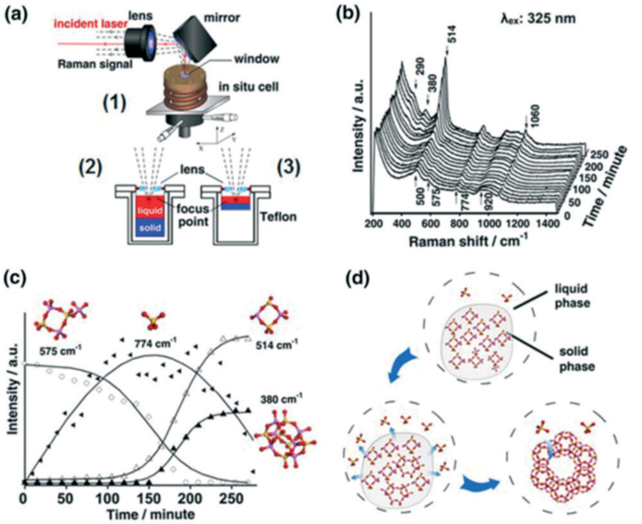

Fig. 12 (a) *In situ* Raman reactor (1) for zeolite crystallisation offering varying focal points (2 and 3); (b) UV Raman spectra (325 nm excitation) during zeolite X synthesis at 373 K; (c) time-dependent evolution of molecular species; (d) proposed mechanism for zeolite X formation, adapted from ref. 37 with permission from Spring Nature, copyright 2015.

2.2.2.1 Zeolite synthesis. Elucidating mechanisms of catalytic synthesis is challenging. Fan *et al.* studied the synthesis of transition metal containing microporous and mesoporous materials using *in situ* UV Raman spectroscopy.[40] The evolution of precursors and intermediates was followed during the synthesis of zeolite X using a hydrothermal reactor specially designed for coupling to a UV Raman spectrometer (Fig. 12a1). A silicon rubber-sealed lens built into the reactor lid enabled laser focusing on to samples, enhancing the Raman signal by 3–4 times that achievable with a plane window. Two sample holders, of different depths, allowed the focal point to be shifted between the liquid phase (Fig. 12a2) and solid–liquid interface (Figure 12a3). Initial spectra (Fig. 12b) showed an amorphous solid phase in equilibrium with monomeric silicate species in the liquid phase (774 and 920 cm^{-1} bands). Four-membered rings and a small amount of branched derivatives (575 cm^{-1} band) were observed during in the early stage of nucleation, whose subsequent disappearance coincided with the emergence of polycyclic structures and zeolite seed crystals (Fig. 12c); these branched derivatives are believed to be a key intermediate in zeolite X formation (Fig. 12d). Such insight could guide the rational design and solution-phase synthesis of porous catalysts.

2.2.2.2 Furfuryl alcohol polymerization. The effect of ethanol on the acid-catalysed polymerisation of furfuryl alcohol (FA) has been studied by time-resolved UV Raman spectroscopy[41] wherein UV excitation circumvented a strong fluorescence background (Fig. 13). For pure furfural (FS1 and FS4), the 1504 cm^{-1} band was characteristic of the symmetric C=C stretch in the furan ring of the monomer, whereas that at 1655 cm^{-1} was indicative of a C=C stretch in the FA polymer. The intensity ratio of these bands, $I_{1654/1504}$, was

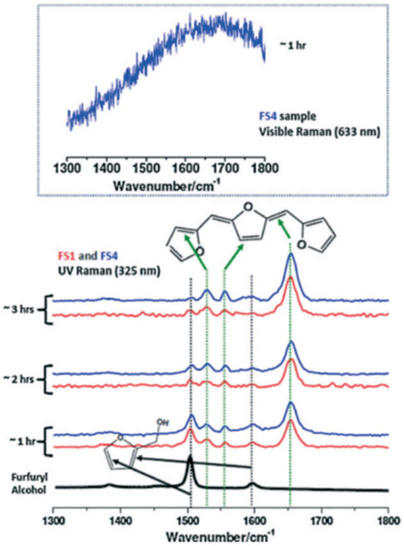

Fig. 13 (left) Raman spectra of furfuryl alcohol (FS1 and FS4) during polymerisation under UV excitation (325 nm) at room temperature and ambient pressure, reproduced from ref. 41 with permission from Elsevier, copyright 2013.

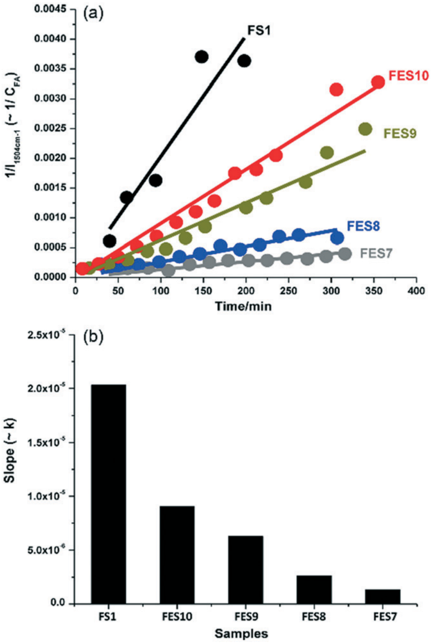

Fig. 14 Effect of ethanol concentration on rate of furfuryl alcohol polymerisation *versus* FS1: (a) $1/I_{1504\text{cm}^{-1}}$ *versus* reaction time; and (b) corresponding second-order rate constant, reproduced from ref. 41 with permission from Elsevier, copyright 2013.

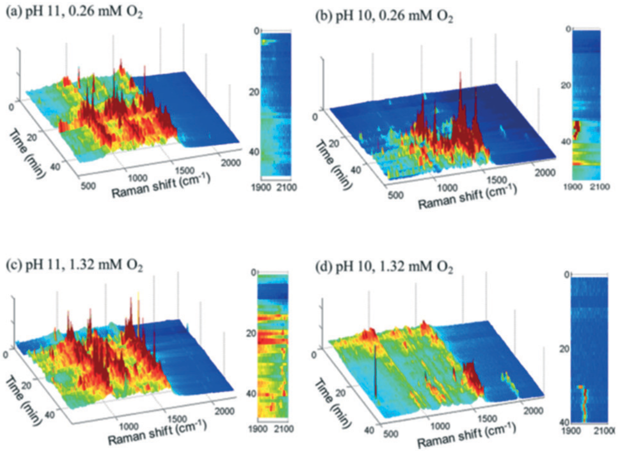

Fig. 15 Time-resolved Au nanoshell SER spectra of 1.3 mM glycerol solutions (a) at pH 11 with 0.26 mM O_2, (b) at pH 10 with 0.26 mM O_2, (c) at pH 11 with 1.32 mM O_2, and (d) at pH 10 with 1.32 mM O_2, reproduced from ref. 45 with permission from the American Chemical Society, copyright 2013.

subsequently employed to obtain quantitative information on the extent of polymerisation in different solvents (Fig. 13). Increasing the ethanol concentration (FES7-FES10), or switching to butanol, inhibited room temperature polymerisation. The time-dependence of $1/I_{1504}$ suggested that polymerisation followed second-order kinetics (Fig. 14).

2.2.3 Surface-enhanced Raman spectroscopy (SERS). Raman scattering is a two-photon process in which only one photon per million is scattered, and consequently the sensitivity of conventional Raman spectroscopy is insufficient to monitor low concentrations of surface species at solid–liquid interfaces. The discovery of surface-enhanced Raman scattering (SERS) by Van Duyne *et al.* therefore represented a significant breakthrough.[42,43] Nanoscale features on metallic surfaces or adsorbed organics can induce signal enhancements of 10^6–10^9 orders of magnitude, although the origin of the phenomena remains debated, with excited localised surface plasmons (electromagnetic theory) and/or the formation of charge-transfer complexes (chemical theory) proposed. Since the discovery of roughened silver electrodes,[44] various substrates have demonstrated SERS, with most associated studies focused on aqueous phase electrocatalytic interfaces.

2.2.3.1 Glycerol oxidation over gold nanoshell catalysts. SERS was applied to study the room-temperature oxidation of glycerol in water and associated role of pH.[45] Au nanoshells were used as both an active oxidation catalyst and SERS enabling substrate, and comprised 100–200 nm silica particles encapsulated by a shell of Au metal several nm thick, which provided SERS enhancements exceeding those of a roughened metal surface (10^8–10^9 *vs.* 10^4). Glycerol oxidation in deoxygenated solutions at pH 11 resulted in SERS features between 800 and 1600 cm^{-1}, with sharp bands ~1000 and 1200 cm^{-1} assigned to oxygen-derived species and that at 1500 cm^{-1} to physisorbed O_2 (Fig. 15a); vibrational bands for the C=O bond of carboxylic acids were not observed. Introducing high concentrations of dissolved O_2 led to the appearance of a weak peak between 1900–2100 cm^{-1}, ascribed to the C–O stretch of chemisorbed CO (Fig. 15c).

SERS indicates that glycerol and glycerolate species do not bind to the catalyst surface in the absence of oxygen, but rather participates in an Eley–Rideal mechanism in which near surface glycerolate reacts directly with adsorbed O_2 or surface bound hydroxyls to form carboxylate species in solution. In addition to deprotonating glycerol, surface hydroxyls increased the surface negative charge on the Au shell, which may enhance O_2 adsorption/activation explaining the high activity of Au-derived catalysts their dependence on basic reaction conditions.

2.2.4 Shell-isolated nanoparticle-enhanced Raman spectroscopy. Shell-isolated nanoparticle enhanced Raman spectroscopy (SHINERS), first reported in 2010, represents an improvement to SERS.[46] This technique requires the synthesis of shell-isolated nanoparticles (SHINs), which are core–shell heterostructures in which SERS-active cores are coated by an ultrathin shell. The shell prohibits any direct catalytic influence from the core by restricting contact with the external chemical environment.[47] Fig. 16 illustrates the operation of SHINs on a single-crystal electrode which provides Raman information on surface species in hotspots. In general, SHINERS probe the region within 20 nm of SHINs, with the strongest enhancement arising in nanogaps between two SHINs or between SHINs and the substrate. The SHINs acts as a signal amplifier, boosting Raman signals from probe molecules.[48]

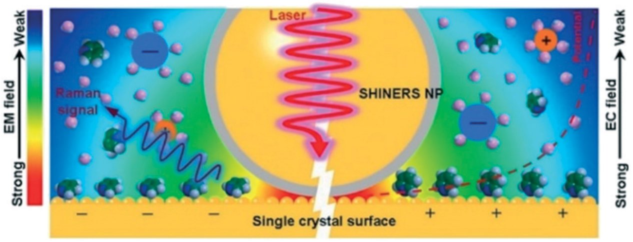

Fig. 16 Operating principle of SHINERS on a single-crystal-electrode surface, reproduced from ref. 48 with permission from the American Chemical Society, copyright 2019.

Formation of surface oxides often hinders electrocatalyst performance, and hence molecular insight into electrochemical oxidation can aid the design of improved catalyst systems. The electrochemical oxygen reduction reaction (ORR) over Pt-based catalyst surfaces is an important challenge for fuel cells research, and the SHINERS technique has been utilised to study this over low-index Pt(*hkl*) surfaces.[49] Fig. 17a shows SHINERS results during the ORR on a Pt(111) surface as a function of applied potential under acidic conditions. Only one Raman peak was observed at 933 cm^{-1} at high potentials, assigned to the symmetric-stretching mode of the perchlorate ion electrolyte, however a second band appeared at 732 cm^{-1} attributed to adsorbed HO_2^* on decreasing the potential to 0.8 V. Under identical conditions, Pt(110) and Pt(100) surfaces exhibited the perchlorate band and Raman features at 1030 and 1081 cm^{-1}, but not the HO_2^* feature (Fig. 17b), and under alkaline conditions only a single Raman peak at 1150 cm^{-1} attributed to superoxide O_2^- anions (Fig. 17c). In conjunction with quantum chemical DFT calculations, the SHINER technique demonstrated that Pt(111) electrodes stabilise HO_2^* whereas Pt(110) and Pt(100) electrodes favour OH*, however under alkaline conditions the ORR reaction occurs over all three surfaces *via* surface O_2^-.

SHINERS was recently adapted to enable *operando* SERS monitoring of electrochemical reactions, extending its application to surface reactions at heterogeneous interfaces. Kim *et al.* placed gold microshells, electrically isolated from an underlying flat Pt electrode by a layers of 11-mercaptoundecanol (MCU) grafted on the microshell surface to perform SERS.[38] The MCU buffer layer facilitates numerous hot spots, without itself participating in the electrochemical reaction (Fig. 18). Such MCU modified gold microshells were used to obtain *operando* Raman spectra during the electrochemical reduction of 4-nitrobenzenethiol (4-NBT) over a flat polycrystalline Pt electrode (Fig. 19). Unreduced 4-NBT was indicated by bands at 1080, 1331 ($-NO_2$ symmetric stretch) and 1570 cm^{-1} (C=C stretching mode). At negative potentials the NO_2 band diminished and the C=C stretch shifted to 1587 cm^{-1} consistent with electrochemical reduction to 4-aminobenzenethiol. Modified gold microshells offer the opportunity to observe interfacial reactions by SERS without restrictions on the electrode structure or material.

2.2.5 Tip-enhanced Raman spectroscopy. In recent decades, tip-enhanced Raman spectroscopy (TERS) has emerged as a powerful nanoanalytical tool for simultaneous

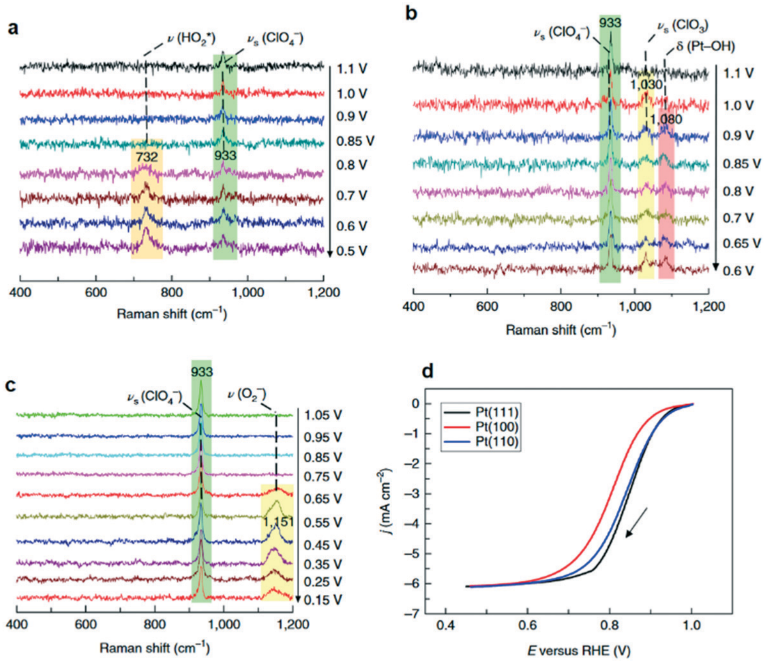

Fig. 17 Electrochemical SHINERS spectra of ORR process over (a) Pt(111) and (b) Pt(110) electrodes in 0.1 M $HClO_4$ solution saturated with O_2, and (c) a Pt(110) electrode in 0.1 M $NaClO_4$ solution (pH ∼ 10.3) saturated with O_2. (d) Polarization curves of the ORR reaction on Pt(*hkl*) rotating-disk electrodes in saturated 0.1 M $HClO_4$ solution, adapted from ref. 49 with permission from Springer Nature, copyright 2018.

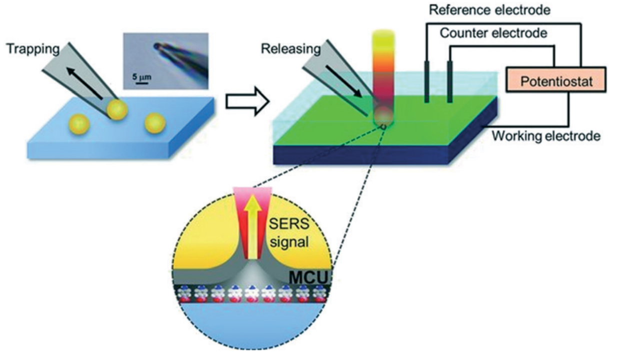

Fig. 18 Schematic showing trapping and placement of individual 11-mercaptoundecanol (MCU) modified gold microshells on a Pt electrode. Upper left: Optical microscopic image of gold micro-shell trapped at the end of a micropipette. Upper right: Electrochemical system with SERS integration; grey layer in the lower part represents MCU self-assembled monolayer on the gold microshell in contact with nitrobenzenethiol molecules, reproduced from ref. 38 with permission from Wiley-VCH, copyright 2013.

topographical and molecular mapping of surfaces. TERS exploits the localised surface plasmon resonance (LSPR),[50–52] wherein an intense electric field is generated at the apex of a metal or metal-coated scanning microscopy probe positioned at the focal point of an excitation laser (Fig. 20).[53] The LSPR between the laser and metal nanoparticles at the probe apex enhances the electric field intensity by several orders of magnitude on a scale confined to the nanoparticle dimensions. To date, the majority of TERS studies have been performed in ambient air or under ultrahigh vacuum conditions but has been rarely applied to aqueous solutions.

2.2.5.1 In situ photocatalytic oxidation of p-aminothiophenol. Weckhuysen and co-workers recently developed a novel atomic force microscopy (AFM)-TERS probe wherein the multilayer metal tip coating was protected by an ultrathin layer of zirconia.[54] This design overcomes TERS limitations such as a short tip lifetime, chemical inertness, and instability in a liquid environment. The zirconia coated (AFM)-TERS probe was used to map the photocatalytic oxidation of a *p*-aminothiophenol (pATP) self-assembled monolayer to *p*,*p*′-dimercaptoazobenzene (DMAB) across a heterogeneous metal surface in water. TERS measurements were performed inside a water droplet on the catalyst surface, which interestingly resulted in a 210 times stronger signal compared to air measurement (Fig. 21). Additionally, their design extended the lifetime of the probes over 850 times while rendering them chemically inert for the investigation of catalytic reactions in the liquid phase. Such improvements

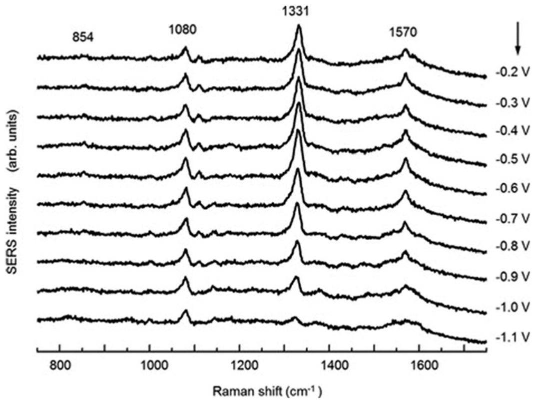

Fig. 19 Potential-dependent SERS spectra of a 4-NBT of adsorbed on a flat Pt electrode in 0.1 M NaOH, reproduced from ref. 38 with permission from Wiley-VCH, copyright 2013.

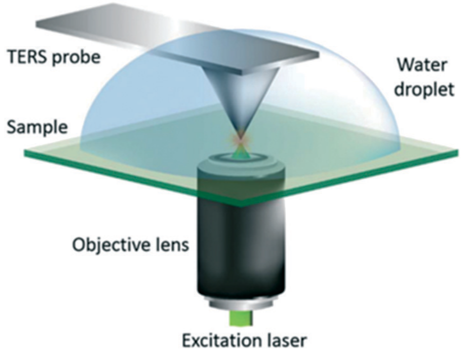

Fig. 20 Schematic diagram of the AFM-TERS system employed. For TERS measurements in liquid, a water droplet was placed on the sample and measurements were performed with the TERS probe fully immersed, reproduced from ref. 53 with permission from the Royal Society of Chemistry, copyright 2018.

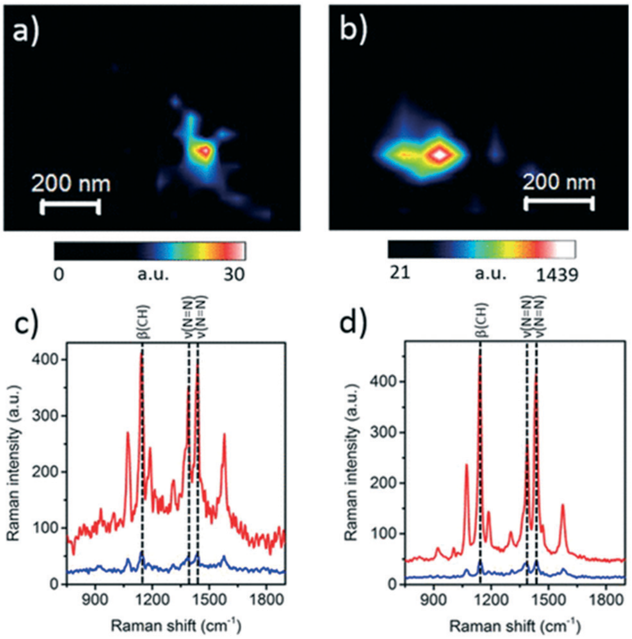

Fig. 21 Maps of pATP → DMAB at the TERS probe apex obtained using the intensity of the 1437 cm^{-1} ($\nu_{N=N}$) DMAB Raman band measured from the pATP self-assembled monolayer on a Ag substrate in (a) air and (b) water. Corresponding TERS (red) and SERS (blue) spectra measured at the position of maximum DMAB signal at the TERS probe apex in (c) panel (a) and (d) panel (b), reproduced from ref. 54 with permission from the American Chemical Society, copyright 2019.

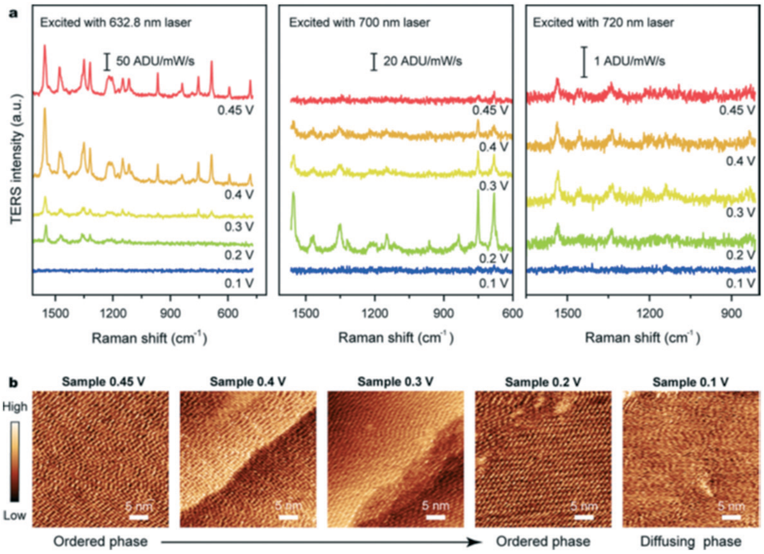

Fig. 22 (a) EC-TERS study of CoPc on Au(111) acquired at different potentials with three excitation wavelengths in 0.1 M $HClO_4$. (b) Sequential STM images of the CoPc adlayer adsorbed on Au(111) at different substrate potentials in 0.1 M $HClO_4$, reproduced from ref. 55 with permission from the American Chemical Society, copyright 2019.

in probe lifetime and structural and chemical stability expand the potential application of AFM-TERS for nanoscale chemical characterization of catalysts under reactive environments.

2.2.5.2 Electrochemical tip-enhanced Raman spectroscopy. Cobalt-derived molecular catalysts are promising candidates for electrochemical reactions such as the ORR. Electrochemical (EC)-TERS was employed to investigate the catalytic activity of cobalt phthalocyanine (CoPc) over Au(111) as a function of substrate potential and excitation wavelength (Fig. 22).[55] The TERS signal was sensitive to both potential and excitation wavelength: under 632.8 nm excitation the Raman intensity was proportional to potential; under 700 nm excitation an inverse relationship was observed; and under 720 nm excitation the intensity was independent of potential. For all excitation wavelengths, no TERS peaks were apparent at 0.1 V. This behaviour was interpreted in terms of CoPc adsorption at the solid–liquid interface. The surface charge density increases with negative potential, weakening the molecule–substrate interaction and inducing an ordered-to-diffuse phase transition (Fig. 22b). During the ORR, the electronic transition of CoPc redshifted from 657 to 700 nm which changes the resonance conditions at different excitation wavelengths. These observations supported a molecular understanding of CoPc catalytic behaviour during the ORR.[55]

2.3 X-ray absorption spectroscopy

X-ray absorption spectroscopy (XAS) can provide invaluable insight into both the electronic and local structural properties of catalytically active species through the excitation and subsequent scattering of core-level electrons.[56] The measurement proceeds through the photoexcitation of electrons most commonly from 1s (K-edge) or 2s/2p (L-edges) into either unoccupied atomic orbitals below or above the Fermi level, or into the continuum at energies significantly above the adsorption edge. This results in two distinct analysis regions associated with X-ray absorption near edge spectroscopy (XANES) and extended X-ray absorption fine structure (EXAFS). XANES, spectra typically extend from ~50 eV before the adsorption edge to ~100 eV above it and provide information on molecular geometry (pre-edge features) and oxidation state (edge position and intensity) and is often used for chemical fingerprinting against reference materials. EXAFS extends from ~100 eV above the adsorption edge to ~1000 eV (depending on the element and core-level), and exhibits features arising from scattering interactions between ejected photoelectrons and neighbouring atoms which provide local structural information (coordination number, neighbouring elements, bond geometry and distances, and disorder). Photon-in/photon-out techniques facilitate *in situ* analysis of catalysts (particularly those containing transition metals interrogable by hard X-rays *i.e.* 5–20 keV) under real-world environments, in contrast to *e.g.* X-ray photoelectron spectroscopy (XPS), wherein vacuum or low pressures are necessary,[57] due to the relatively weak attenuation of X-rays *versus* low energy electrons. However, although the penetrating nature of (particularly hard) X-rays is beneficial for investigating catalysts within fluids, and active sites at buried interfaces or within porous architectures, a caveat is that transmission and fluorescence XAS detection are not surface sensitive, indeed spectral contributions may be a summation over several thousand nanometers of material. Analysis of highly dispersed nanoparticles (a few nms diameter), clusters and single sites offers an indirect means to impart surface sensitivity, through increasing the proportion of surface atoms in the catalytically phase. Alternatively, X-ray excited Auger and secondary scattered electrons can provide direct surface sensitive information through total electron yield (TEY) detection.[58] TEY requires either the detection of such electrons either near to the surface (prior to their absorption by surrounding media, necessitating vacuo/near ambient pressure configurations[59]), or measurement of the compensating current by a picoammeter wherein the catalyst is part of an electrical circuit. In both configurations TEY gives spectral information from the first few nanometres (≤3 nm) of a catalyst surface due to the short electron escape depth.[60] Soft X-rays (∼0.1 to 3 keV) have also been used to study catalyst surfaces, allowing K-edge measurements of light elements *e.g.* C, O and N (common reactants/products) and S, P, Cl (common active site poisons), and L and M edges of 1st and 2nd row transition metals respectively.[61] As with hard X-rays, the sampling depth for X-ray detection depends on the photon mean-free path, which for soft X-rays is *ca.* 100 nm[62] necessitating thin samples, on the order of tens of nanometers, and gas environments.[59] Historically, such measurements have been the domain of synchrotron radiation sources, in part due to their provision of tunable and high brilliance X-ray photon energies,[63] however, laboratory XAS instruments have enjoyed a recent resurgence driven by the development of commercial systems exploiting bremsstrahlung radiation from modern X-ray tubes.[64,65]

2.3.1 Applications and limitations. The application of XAS to *operando* catalyst studies has been enabled through advances in synchrotron radiation, notably the increased brilliance of 3rd generation light sources (further enhancements are anticipated from forthcoming 4th generation sources) and the design and development of X-ray optics alongside high sensitivity and dispersive detectors. Reaction cells for *in situ*/*operando* gas phase measurements, typically comprising a heated capillary or windowed furnace attached to a gas manifold, can be readily integrated into most synchrotron beamline hutches. These have provided unique insight into the active sites of working catalysts, *e.g.* the critical role of hydride and carbide formation during gas-phase alkyne hydrogenation over at ambient pressure,[66,67] the synergy, stability and redox character of active sites in bimetallic methane reforming catalysts,[68,69] the role of active sites and promoters Co catalysed high pressure Fischer–Tropsch synthesis,[70] and the effect of pressure and particle size on silver catalysed acrolein hydrogenation.[71,72] More sophisticated reaction cells permit the integration of multiple analytical techniques. For example, XAS/DRIFTS/MS studies of Al_2O_3-supported $Rh^I(CO)_2Cl$ revealed reversible conversion to monodispersed Rh nitrosyl species under NO and CO respectively,[73] restructuring of Pd nanoparticles in three-way catalysts under oxidising and reducing environments[74,75] (subsequently identified by HXRD studies as arising from PdC_x formation[76]), formation of a 2D $Ag_n^{\delta+}$ species during selective catalytic reduction of NO,[77] and active site stability/restructuring during alcohol oxidations.[78]

In contrast, *operando* XAS studies of liquid phase catalysts are rarer, in part reflecting stronger X-ray absorption by the reaction media, especially for halogenated solvents, but also due to added complexity in the reactor design. Nevertheless, valuable insight has been obtained for example, the nature of catalytically active sites and deactivation mechanisms in the liquid phase selective aerobic oxidation of alcohols over Pd catalysts.[79,80] Although such measurements can be conducted at ambient pressure, thereby simplifying the experimental set-up and use of standard commercial or in-house reaction cells. In contrast, selective hydrogenations typically require elevated hydrogen pressure, and hence bespoke autoclaves in which high-pressure reactions can be conducted in concert with the collection of X-ray spectra are required.[81] Additional engineering challenges for liquid phase XAS measurements include interfacing multiple techniques to mirror the gas phase experiments described above, and rapidly changing the reaction environment to permit modulation excitation experiments. Strong attenuation by the reaction media and reactor windows is also particularly problematic for catalysts requiring soft(er) X-rays. Microfluidics[82] and/or the development of novel window materials with high X-ray transparency such as graphene and beryllium[83] are possible solutions, and will benefit from increases in brilliance, through the roll-out of 4th generation synchrotron sources,[84] and detector sensitivity, and further improvements in X-ray optics.[85] Together these will afford greater sensitivity for active species and promotors at realistic concentrations (ppm to ppb levels), and improved temporal and spatial resolutions moving to sub-milli/microseconds and sub-μm respectively; such progress is necessary to elucidate quantitative structure–reactivity relations, map active site/promoter/poison distributions, and evaluate active site leaching/migration.

Examples of liquid phase *operando* XAS will be discussed to highlight the current state-of-the-art and inspire future investigations particularly in renewable energy and sustainable chemistry.

2.3.2 Alcohol selective oxidation. *Operando* XAS has been extensively used to elucidate the nature of the active catalytic species in the selective oxidation (selox) of alcohols over Pd nanoparticles. Preliminary investigations by different groups provided contradictory proposals for the reaction mechanism, with both oxide and metal active sites inferred. *In situ* reduction of PdO_x observed during cinnamyl and benzyl alcohol selox over a Pd/Al_2O_3 catalyst was taken by Grunwaldt and co-workers as evidence of a metal active site, however parallel kinetic studies were not performed, prohibiting the determination of structure–activity relationships.[86,87] In contrast, related studies by the same group using supercritical CO_2 as the solvent suggested a partially oxidised palladium surface was optimal.[88] Prior[89,90] and concurrent kinetic and *ex situ*/*operando* XAS studies by Lee and co-workers on cinnamyl alcohol selox over Pd/C and Pd/Al_2O_3 catalysts strongly supported a PdO_x active site,[79] a hypothesis strengthened by subsequent *in situ* XPS,[91,92] and

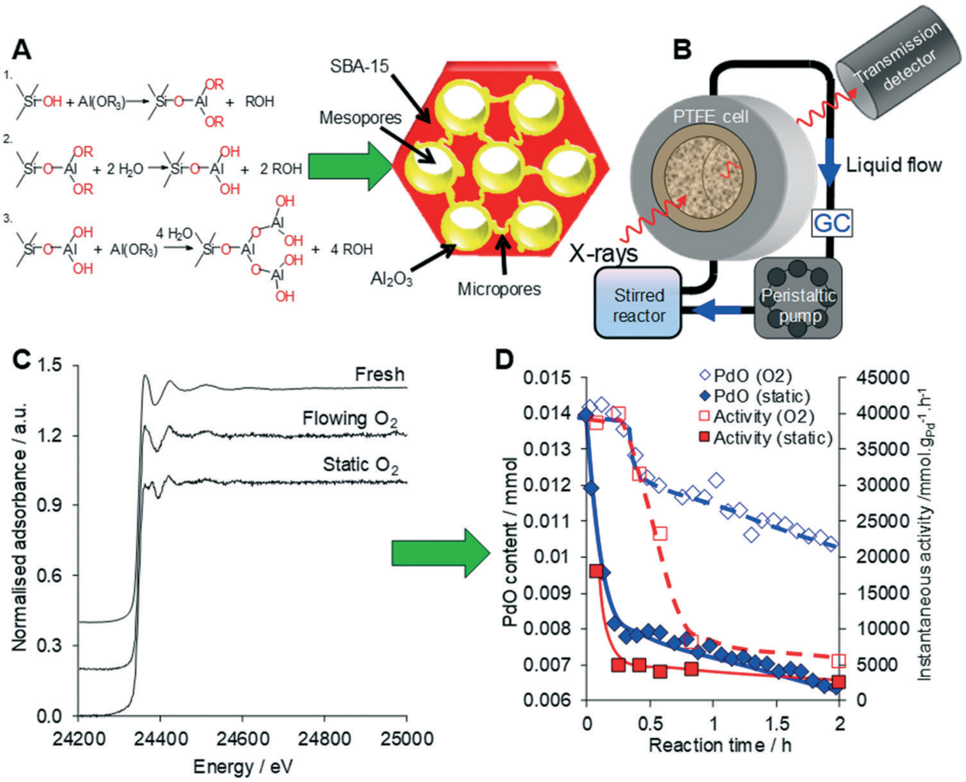

Fig. 23 (A) Synthesis of a conformal adlayer of alumina over a mesoporous SBA-15 silica framework. (B) *Operando* liquid phase XAS setup. (C) Liquid phase *operando* Pd K-edge XAS of Pd/Al_2O_3-SBA-15 during cinnamyl alcohol selox. (D) Correlation between PdO concentration from XAS and selox activity under static *versus* flowing oxygen. Modified from ref. 80 with permission from Elsevier, copyright 2014.

vapour phase dynamic XAS studies in the absence of solvent effects.[78,93,94] These conclusively established surface PdO_x as the active site, most likely through a Mars–van Krevelen mechanism in which molecular oxygen replenishes oxygen adatoms abstracted by hydrogen adatoms during oxidative dehydrogenation of the alcohol. Such insight enabled the subsequent development of high performance single atom[95] and supported Pd catalysts (Fig. 23A) wherein the concentration and stability of PdO_x species was optimised. Liquid phase *operando* XAS, employing a simple recirculating set-up to mirror batch reactor kinetics (Fig. 23B) further were also consistent with an oxide active site, and identified *in situ* reduction of PdO_x to Pd metal as the primary deactivation pathway (Fig. 23C and D).[80] Supported Ni NPs have also been investigated for aldehyde production *via* the 2-octanol dehydrogenation; *operando* XAFS revealing a synergistic mechanism between NiO sites and $Ni^{\delta+}$–$O^{\delta-}$ acid–base sites.[96] Although alcohol selox over earth-abundant metals is desirable, the resulting turnover frequencies remain much lower than for precious metals, even at elevated reaction temperature.

Allylic alcohol selox has also been investigated by Scott and co-workers through Pd L_{III}-, P K- and Au L_{III}-edge XAS to probe the nature of PVP-stabilised AuPd colloidal nanoparticles. *In situ* XAS measurements necessitated the use of a bespoke PEEK cell with Kapton windows alongside commercial XRF liquid cells, with X-ray attenuation minimised through judicious choice of cell windows. XAS studies revealed the critical role of sequential reduction of the bimetallic nanoparticles during catalyst synthesis, which resulted in an electron-deficient Pd-enriched surface over a Au core.[97] *In situ* XAS was also used to study the synthesis of a AuPd bimetallic catalyst from a $Pd^{(II)}$ salt in the presence of crotyl alcohol. Two possible mechanisms were hypothesised: (i) redox cycling of $Pd^{(2+)}$ and $Pd^{(0)}$, in which $Pd^{(0)}$ deposition from K_2PdCl_4 was driven by the alcohol reductant, evidenced by concomitant crotonaldehyde formation, and subsequent dissolution of $Pd^{(2+)}$ from the Au surface driven by reaction with O_2; or (ii) an entirely heterogeneous pathway in which the adsorbed alcohol reacts with electron-deficient Pd surface atoms to form the allylic aldehyde *via* β-hydrogen elimination. The stability of the Pd oxidation state from Pd L_{III}-edge XAS studies upon introducing oxygen to the reaction solution favours the heterogeneous mechanism.[98]

2.3.3 Selective hydrogenation. Selective hydrogenation typically requires elevated hydrogen pressures, at least in part to improve gas solubility in the reaction medium, and as noted above this has hindered the development of liquid phase reaction cells. *Ex situ* XAS studies have attempted to elucidate the active species in liquid phase hydrogenation, such as the role of bimetal Co, Cu and Sn promoters in controlling C=O *versus* C=C hydrogenation in Pt/SiO_2 catalysed cinnamaldehyde and crotonaldehyde reduction,[99,100] charge transfer in active sites for biomass-

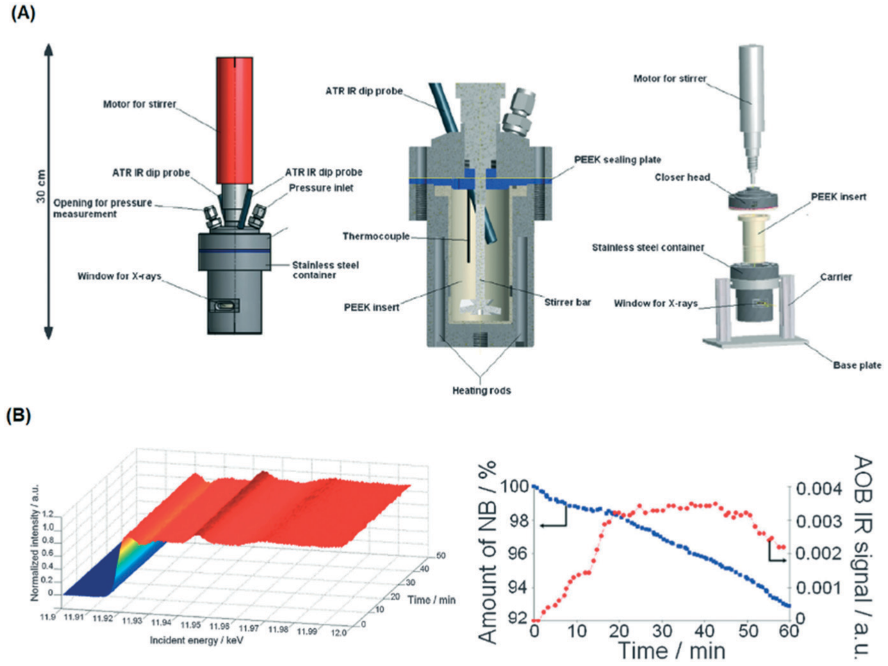

Fig. 24 (A) HERFD XAS/ATR-FTIR autoclave schematic. (B) (left) Time-dependent Au L_{III}-edge HERFD XAS and (right) nitrobenzene (NB) and azoxybenzene (AOB) concentrations during aqueous phase hydrogenation over Au/CeO_2 under 10 bar H_2. Reproduced from ref. 81 with permission from the Royal Society of Chemistry, copyright 2012.

derived substrate hydrogenation in ambient pressure,[101] and the presence of metallic Au in structure-sensitive hydrogenation of and the presence of metallic Au in structure-sensitive hydrogenation of nitroaromatics.[102] *In situ* XAS gas phase measurements before and after 773 K reduction in flowing H_2 provided some insight the influence of Co on the electronic properties of Pt in bimetallic alloy nanoparticles for citral hydrogenation.[103] Although the latter represents a significant improvement on *ex situ* characterisation, the low H_2 pressures (ambient *versus* 10 bar during kinetic studies) and absence of solvent/reagent(s) during XAS analysis limits the utility of such measurements.

To address this, van Bokhoven and co-workers constructed a bespoke autoclave reactor capable of simultaneous XAS and ATR-IR (*via* a fibre optic dip probe) measurement (Fig. 24) for high pressure hydrogenation.[81] This was applied to study the evolution of a Au/CeO_2 catalyst during nitrobenzene hydrogenation. A metallic Au active phase was identified, and ATR-IR revealed a stepwise reaction *via* an azoxybenzene intermediate. The same *operando* XAS reactor has been used to evaluate: the effect of Au particle size on nitrobenzene hydrogenation;[104] shifts in the Fermi level of Pt nanoparticles due to allylic carbonyl adsorption (during aldehyde reduction) as a descriptor of catalyst selectivity;[105] and the mechanism of $Pd^{(2+)}$ reduction and aggregation within a $[Pd(2\text{-pymo})_2]_n$, (2-pymo = 2-pyrimidinolate) metal–organic framework during 1-octene hydrogenation at 2 bar H_2.[106] Continuous flow high pressure (22 bar) furfural hydrogenation within a glassy carbon reactor tube[107] enabled observation of on-stream sintering of Cu nanoparticles and resulting catalyst deactivation.[108]

2.3.4 Hydrogen peroxide synthesis. Hydrogen peroxide is an important industrial oxidant whose use results in water as the sole by-product, and hence, if synthesised itself through a clean process, supports the development of sustainable chemical processes. Unfortunately, commercial H_2O_2 production currently proceeds by the anthraquinone process, which is only economically viable at large scale and high concentrations, producing significant waste and posing hazards in handling, storage and use. There is therefore great interest in developing catalytic systems for on-demand and small scale H_2O_2 production (and at lower concentrations).[109] Three-phase (H_2, O_2, H_2O or methanol and catalyst) *operando* XAS studies of heterogeneous catalysts for the H_2 + O_2 reaction required the development of a bespoke plug flow reactor capable of gas and liquid phase reactions up to 80 °C and 7 bar and suitable for transmission and fluorescence XAS.[110,111] Stainless steel construction afforded diverse applications, excepting the use of mineral acids, however, the fixed reactor diameter and hence pathlength is not optimal for all photon energies.

This reaction cell was evaluated for H_2O_2 production from H_2 and O_2 (diluted in CO_2) in methanol over a commercial Pd catalyst, however a lack of quantitation of the catalytic reaction prohibited determination of structure–reactivity relationships. Despite this, Pd K-edge fluorescence spectra evidenced the ability of Br^- to promote reduction of PdO to Pd metal and concomitant leaching, which improves peroxide selectivity. *Ex situ* XAS measurements on Pd/TiO_2 systems also postulated roles for both Pd metal and oxide, speculating that the interface between these phases was

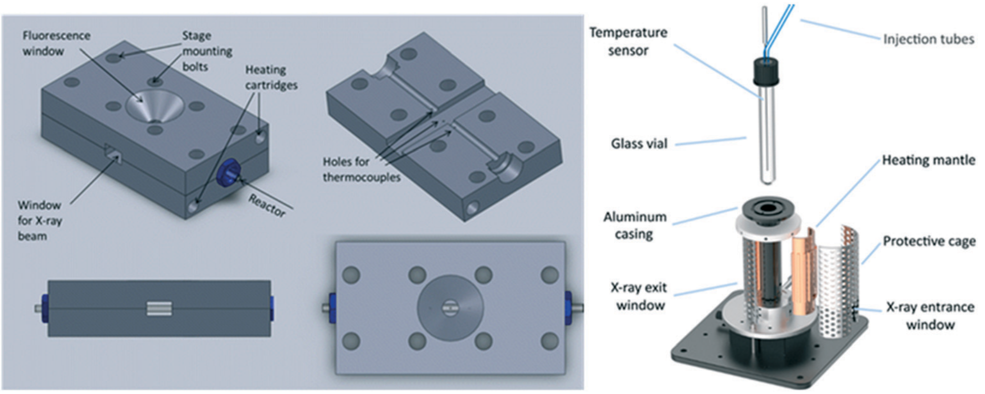

Fig. 25 (Left) Schematic of high-pressure continuous flow XAS cell. (Right) Bespoke reactor for combined *operando* XAS and PXRD measurements, reproduced from ref. 114 and 126 with permission from the American Chemical Society, copyright 2012 and 2018 respectively.

responsible for optimal H_2O_2 productivity.[112] Grunwaldt and co-workers commissioned a similar continuous flow reactor, but in which spectra could be collected at different positions along the catalyst bed and capable of pressures up to 10 bar. Liquid phase H_2O_2 synthesis in water saturated with H_2 and O_2 (from separate streams) was evaluated over Pd/TiO_2 in the presence of Br^- promotor, and similarly identified the presence of Pd metal and oxide phases, attributed to a metal core@oxide shell structure. Under reaction conditions, the core was transformed to Pd hydride, with the hydride phase (α or β) dependent on the $H_2:O_2$; however H_2O_2 production was only associated with α-PdH.[113] Bimetallic AuPd nanoparticles were also screened for H_2O_2 production continuous flow within a microfluidic reactor, wherein PdH_x was also observed. In the latter case, it was postulated that hydride was inactive (although which phase is unclear), with Pd metal proposed as the active species with Au prohibiting hydride formation.[82]

2.3.5 Aqueous phase reforming. Wang and co-workers reported a bespoke *operando* continuous flow reactor capable of working under industrially relevant conditions of up to 400 °C and 75 bar (Fig. 25).[114] Utilising this set-up they investigated the active species in APR of glycerol (a potential feedstock for bio-derived chemicals) over Pt/C; sintering of Pt nanoparticles occurred during reaction, and both activity and selectivity were strongly influenced by the solution pH. C–O cleavage increased at both low and high pH, being favoured under acidic conditions, XANES measurements indicating that HNO_3 enhanced H_2 adsorption and supressed CO adsorption over Pt. The same reactor has been used to identify the origin of Re promoted aqueous[115] and steam reforming[116] of glycerol over Pt/C through the formation of ReO_x species and spillover and facile desorption of reactively-formed CO from neighbouring Pt sites. *Operando* XAS of glycerol APR over bimetallic PtMo/C catalysts revealed a Pt core@Mo shell structure wherein a small proportion of surface Pt metal is stable during catalysis and likely responsible for the high H_2 selectivity.[117]

2.3.6 Carbon–carbon couplings. Aryl–aryl and heteroaryl C–C bond-forming reactions are central to modern synthetic organic chemistry and have long been considered the domain of homogeneous catalysts. However, there is a precedent for (apparent) surface catalysed C–C coupling, which *operando* XAS has been pivotal in investigating.

The Suzuki–Miyaura cross-coupling of iodonanisole and phenylboronic acid by PVP-stabilised Pd nanoparticles was studied by *operando* XAS in a bespoke PTFE cell to evaluate whether Pd leaching (and associated homogeneous catalysis) occurred during reaction.[118] Under mild reaction conditions, the Pd–Pd coordination number remained constant, indicating a common size and negligible dissolution from low coordination edge and corner sites of nanoparticles, which in conjunction with kinetic and spectroscopic studies,[119] provided strong evidence for a purely heterogeneous active site. *In situ* liquid phase XAS measurements also identified $Pd^{(0)}$ clusters as the active phase for ligandless Suzuki–Miyaura cross-coupling of 4-chlorobromobenzene and 4-fluorophenylboronic acid.[120]

Hii and co-workers also studied the stability of supported Pd nanoparticles during Suzuki–Miyaura cross-coupling by *operando* K-edge measurements along a packed catalyst bed under continuous flow. Herein, hot flowing ethanol resulted in Pd dissolution and subsequent downstream redeposition as metallic Pd nanoparticles,[121] an important observation given the widespread use of ethanol as a solvent/reactant,[122] and medium for catalyst preparation and characterisation.[123] Pd/Al_2O_3 catalysts have also been evaluated for enantioselective allylic alkylation of (*E*)-1,3-diphenylallyl acetate, and Heck coupling of bromobenzene with styrene.[124,125] Catalyst stability in the former reaction was dependent on the Pd oxidation state, with $Pd^{(2+)}$ leaching exacerbated under oxidising (air) environments or halogenated solvents thereby opening the possibility of a homogeneous pathway, while deactivation in the latter reaction coincided with formation of a bromopalladate complex. Heck coupling has also been evaluated over Pd@MOF catalysts by *operando* XAS and PXRD within a bespoke batch reactor (Fig. 25).[126] Migration and agglomeration of Pd within the MOF collapsed the porous framework, however this was not responsible for catalyst deactivation, which rather occurred through halide poisoning and site blocking of Pd clusters.

2.4 X-ray photoelectron spectroscopy

X-ray photoelectron spectroscopy (XPS) permits elemental quantification, and information regarding the oxidation/chemical state and electronic band structure of materials, and in some cases their structural arrangement.[127] The technique involves photoexcitation of a core (or sometimes valence) electron, typically using soft X-rays (0.1 to 3 keV) and measurement of the kinetic energy of resulting photoelectrons ejected from a material. XPS is an inherently surface sensitive technique due to the relatively short inelastic mean free path (λ) of emitted photoelectrons, which usually span 0.1 to 2 nm, and hence has found routine application in heterogeneous catalysis where surface phenomena dominate.[57,128]

2.4.1 Applications and limitations. Since XPS requires detection of an emitted photoelectron, it was historically performed under ultra-high vaccum (UHV) conditions, rendering it inefficient as a probe of solid–liquid interfaces where vapour pressures would compromise the necessary vacuum. However, efforts to perform XPS at higher pressures are as old as the technique itself, with gradual technological improvement facilitating higher pressures from 0.1 mbar[129] up to the development of a differential pumping system[130,131] permitting near ambient pressure (NAP) analysis suited to probing solid–vapour and solid–liquid interfaces.[132–134] Despite commercialisation of NAP-XPS technology, the majority of catalytic studies remained focused on solid–gas interfaces, largely due to experimental limitations arising from the higher density of liquids *versus* gases and concomitant increased photoelectron attenuation.[135] Early methods of solid–liquid interface analysis included dipping and drying,[136] in which aqueous electrolytes were deposited on a sample under an applied potential, dried and placed in an XPS system. This facilitated analysis of the electric double layer (EDL) which remained in place following solvent evaporation, but is not an *operando* technique since it only captures a singular point in time at equilibrium. The technique was subsequently refined into a 'dip and pull' method[137,138] in which a submerged sample was slowly removed from the electrolyte solution under NAP conditions, facilitating *operando* study, however concerns remain regarding mass transport limitations in this approach.[138,139] Relative humidity control within a NAP-XPS system facilities the formation of ultrathin layers of liquid (a few nm) atop a solid, allowing analysis of a solid–liquid interface possessing a more bulk-like liquid than for the single EDL method; however, the liquid film must be kept sufficiently thin to minimise attenuation of photoelectrons emitted by the underlying solid–liquid interface and solid.[140,141] Achieving such ultra-thin liquid layers requires a high degree of control over experimental conditions and is impractical in many cases, but was successfully used to probe Pt polymer electrolyte fuel cell systems in *operando*.[142,143]

A major drawback of the aforementioned techniques is the necessity of 'tender' or 'hard' X-rays (approximately 2 keV to 7 keV) to produce photoelectrons able to escape the liquid layer. Such X-rays have reduced photoionisation cross-sections for lighter elements and can result in spectra dominated by the underlying catalyst surface.[139] Liquid jets, which have a rich history of application to study pure liquids,[144] have also been used to study solid–liquid interfaces. Addition of SiO_2 nanoparticles to a liquid stream enabled analysis of the local charge density at the water/silica interface.[145] Such methods may also utilise soft X-rays, but with greatly diminished signals, and tend to be more effective for photon energies >2 keV. They also require highly specialised equipment and a dilute suspension, which may be problematic for low loading catalyst systems. *In situ* cells can exploit pressure differentials between UHV and liquids across a Nafion® proton exchange membrane to transport vapour and target molecules to catalyst surfaces for analysis.[146] Such liquid–solid layers permit *operando* measurements of electrocatalysts, revealing surface species present in the oxygen evolution reaction (OER) over Pt[146] and Ir[147] electrodes. Potentially the most promising technological advance for liquid–solid XPS studies is the use of graphene-based cells (Fig. 26),[148] wherein the high mechanical strength of ultra-thin graphene sheets/nanobubbles offer good signal quality using soft X-rays at pressures reaching 1 bar, even under continuous liquid flow.[149,150] Such systems have exhibited excellent sensitivity even at photon energies as low as 275 eV.[149] The use of graphene in the cell architecture renders such cells ideal for *in situ* studies of metal–graphene catalysts for OER.[150,151] For example, the observation of carbonyl-like hybrid interfaces forming *in situ* between Co and graphene has helped identify the electrocatalytic active site.[151] Deposited nanoparticle catalysts can also be interrogated in the liquid phase by this approach, unlocking diverse applications across heterogeneous catalysis.[152] Graphene nanobubbles have also been utilised to study the *operando* thermal reduction of $FeCl_3$ to $FeCl_2$ in aqueous solution, although improved flow capabilities are desirable.[153] Production of graphene windows is time- and

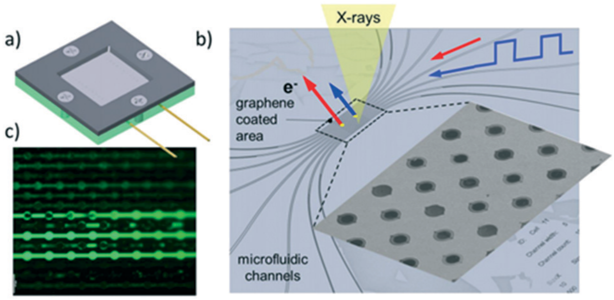

Fig. 26 Fluidic multichannel graphene cell for photoelectron spectroscopy under UHV conditions. a) Overall design; b) SEM image of water filled micro-channels with graphene capped orifices; c) fluidic tests with fluorescein dye, reproduced from ref. 148 with permission from Cambridge University Press, copyright 2018.

labour-intensive and remains a significant hurdle to wider adoption for real-time solid–liquid catalysis.

2.5 UV-vis spectroscopy

The use of UV-vis spectroscopic in catalytic reactions is challenging: it usually does not provide unequivocal information on molecular structure, bands are often broad and suffer from interference by minority species hindering spectral interpretation, and quantitation may be impossible due to a lack of molar absorption coefficients. There are few studies on the application of UV-vis spectroscopy in solid–liquid catalysis, and these are typically in conjunction with complementary techniques to help differentiate possible structures. Some examples of time-resolved UV-vis spectroscopic studies of heterogeneously catalysed liquid phase reactions are described below.

2.5.1 Alcohol oxidation over Pd/Al_2O_3. Selective aerobic oxidation of alcohols is an attractive synthetic route for fine chemicals production. A combined IR/UV-vis study of alcohol oxidation over a Pd/Al_2O_3 catalyst yielded information on the chemical nature of dissolved and adsorbed species (ATR-IR) and the electronic properties of active sites (UV-vis).[154] An ATR-IR flow cell was adapted to include a fused silica window enabling the simultaneous recording of UV-vis and IR spectra of the catalyst layer and reactor product stream. A UV-vis probe was positioned in front of the window, perpendicular to the IRE surface, such that the probe tip was a few millimeters above the catalyst. The solvent was saturated with gases from glass bubble tanks and flowed over the catalyst by a peristaltic pump (Fig. 27) to periodically introduce ethanol saturated with hydrogen or oxygen during synchronous ATR-IR and UV-vis spectral acquisition. Several species were identified at the catalyst–liquid interface by ATR-IR during ethanol oxidation, which proceeded by acetaldehyde and subsequent acetic acid production (indicated by IR bands associated with acetate on the Al_2O_3 support). Reactively-formed CO was also observed on the Pd nanoparticles due to acetaldehyde decarbonylation. UV-vis evidenced reversible changes in the Pd oxidation state on switching between O_2 and H_2 saturated ethanol streams, superimposed on a gradual irreversible change in UV-vis spectra during the oxygen treatments attributed to slow Pd dissolution.[154]

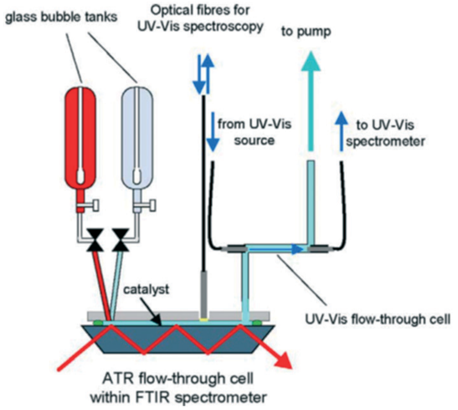

Fig. 27 Schematic of continuous flow reactor for simultaneous *in situ* ATR-IR and UV-vis analysis during ethanol oxidation over Pd/Al_2O_3, reproduced from ref. 154 with permission from Elsevier, copyright 2005.

2.5.2 Gas–liquid–solid reactions. Three phase reactions wherein both gas–liquid and solid–liquid interfaces co-exist present especial challenges to obtaining reliable spectroscopic information from heterogeneous catalysts.[155] Nijhuis and co-workers reported the use of UV-vis spectroscopy to measure insoluble pH indicators adsorbed on solid surfaces in a particle slurry, a packed bubble column and trickle bed reactor. Insoluble pH indicators were adsorbed on the surface of a solid support possessing a high reflectance (such as Al_2O_3 or TiO_2) to simulate an active catalyst, and thereby determine UV-vis spectra in multiphase systems. This study sought to remove spectral interferences (such as those arising from bubbles) and hence enable isolation of signals solely from adsorbates (Fig. 28). For the slurry reactor, UV-vis spectra from moving particles was used to determine the indicator transition point and particle concentration. A new tolerance-and-averaging method was developed to remove UV-vis spectral interference from the pH indicator adsorbed at the solid surface arising from disturbances caused by bubbles in the packed bubble column. It is important to note that liquid films flowing over solid surfaces did not interfere with UV-vis spectra, and hence this reactor configuration is optimal for *in situ*/*operando* studies of heterogeneous catalysts.[155]

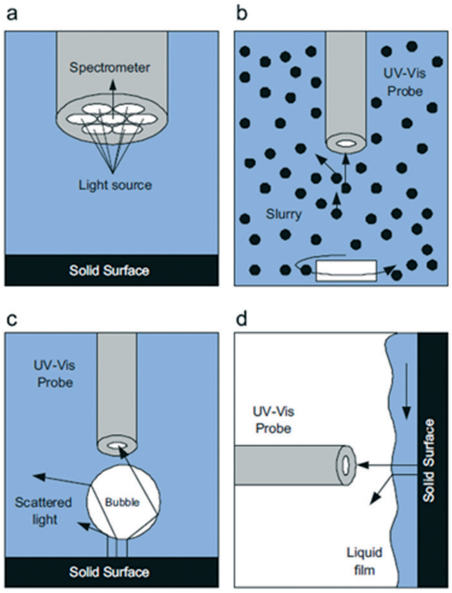

Fig. 28 a) Details of the optical probe tip and schematic representations during *in situ* UV-vis analysis, (b) in a slurry reactor, (c) a packed bubble column, and (d) a trickle bed reactor, highlighting interferences at the gas–liquid and solid–liquid interfaces that scatter light away from the optical probe, reproduced from ref. 155 with permission from Elsevier, copyright 2010.

2.6 Second-order nonlinear optical spectroscopy

Sum frequency generation (SFG) vibrational spectroscopy (VS) is one of few techniques able to provide molecular information at the solid–liquid interface that is directly relatable to catalytic activity.[156,157] This is a consequence of selection rules which allow molecules in a centrosymmetric environment in the bulk (liquid) media to be differentiated from those at a surface. In SFG-VS, visible and IR lasers are simultaneously focused on the interface of interest. An optical (SFG) signal is generated by combining the visible and IR light in a predetermined direction to the interface. This SFG signal is resonantly enhanced when the IR frequency is tuned across the frequency of a molecular vibration, thereby isolating the vibrational spectra of molecules at an interface[156,157] which can be combined with computer modelling to determine absolute molecular orientations. However, SFG-VS is challenging since large, non-resonant signals from metallic and semiconductor surfaces can obscure the weaker molecular fingerprint,[157] and for thick (opaque) substrates, a thin solvent layer is required to obtain data on adsorbates.[158] Improved modelling of the interfacial refractive index is also required to derive more accurate experimental spectra. Some examples of SFG-VS applied to liquid phase heterogenous catalysis are discussed below.

2.6.1 Carboxylate adsorption. Carboxylate is a common modifier of nanoparticles surfaces, and its adsorption from aqueous solution over CeO_2 nanoparticles was studied by *in situ* SFG-VS to identify the binding mode.[159] CaF_2 was used as an optical substrate to enable direct SFG-VS measurement of carboxylate ligand binding over ceria nanoparticles which revealed two distinctive bidentate adsorption modes: a bridging carboxylate characterised by a 1440 cm^{-1} band, and chelating carboxylate by a band at 1475 cm^{-1} (Fig. 29).[159] These bidentate modes co-exist on partially reduced ceria surfaces, whereas the bridging mode dominates over oxidised ceria. DFT calculations suggest that dissociative adsorption is more favourable at highly undercoordinated corner sites on model ceria clusters compared to the sites on a flat surface. SFG-VS is a powerful tool to directly characterise reactions and adsorption processes at nanoparticle interfaces in aqueous solution.[159]

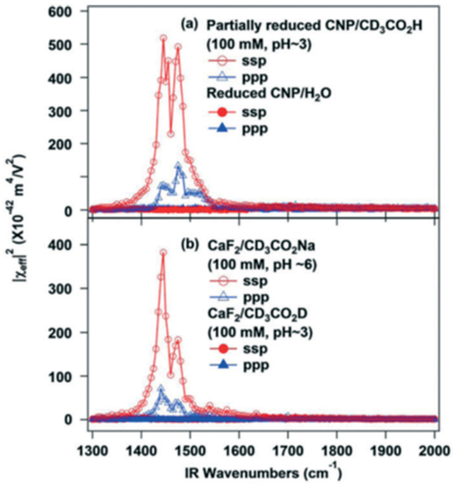

Fig. 29 SFG-VS spectra of (a) partially reduced ceria nanoparticles in contact with water or a CD_3CO_2H aqueous solution (pH ∼ 3), and (b) bare CaF_2 substrate in contact with either CD_3CO_2H (pH ∼ 3) or CD_3CO_2Na (pH ∼ 6) aqueous solutions, reproduced from ref. 159 with permission from the American Chemical Society, copyright 2013.

2.6.2 Electro-oxidation of ethanol. SFG-VS has also been used to investigate the ethanol/platinum interface in acidic aqueous solution, in conjunction with DFT calculations to identify the surface intermediates during ethanol electro-oxidation.[160] A wide range of hitherto unreported adsorbed intermediates were observed including η^2-acetaldehyde, η^2-acetyl, ethylidyne, monodentate acetate, methoxy, tertiary methanol derivative, η^2-formaldehyde, mono and bidentate formate, and COH, CH_3 and CH_2 residues. Evidence was also demonstrated for an ethoxy intermediate, secondary ethanol derivative and acetyl, indicating that the surface chemistry of Pt is much richer than previously considered.

3. Conclusions

In situ and *operando* techniques can provide unique and often invaluable insight into catalytic reaction mechanisms, the nature of active and spectator species, and deactivation pathways in liquid phase heterogeneous catalysis. Such studies have been facilitated by the design and development of advanced catalytic reactors and their integration with time- and spatially resolved spectroscopies which have been enabled by modern synchrotron radiation facilities.

A molecular level understanding of reaction mechanisms at the solid–liquid interface requires careful kinetic analysis and correlation between evolving physicochemical properties and adsorbed species. For kinetic studies, quantitative analysis of spectra is required, however this is not trivial, and in practice studies often result in empirical/semi-empirical correlations between signal intensities and concentrations of species for individual techniques. To improve the accuracy of kinetic information, and hence reliability of associated models, calibration of the detected signal intensities is essential. The combination of multiple *in situ*/*operando* techniques such as ATR-IR or Raman with UV-vis and/or scanning probe techniques in a single experimental configuration improves the reliability of kinetic information and affords greater insight into chemical processes. There are many authoritative articles and texts that compare such complementary spectroscopies.[9,161]

Studies of structure–activity relationships in solid catalysed liquid-phase reactions require careful consideration of multiple interactions at the solid–liquid interface including solvation, adsorption, and intermolecular bonding. In porous catalysts such as zeolites, the solvent composition can significantly affect the concentration of reactants throughout the pore network and compete for acid sites during reactions. In electrocatalysis, the concentrations of species at the electrochemical interface may differ substantially from those in the bulk media. Quantitative understanding of mass transport and solvation effects near the electrode surface are therefore important to develop meaningful models of electrode-mediated reactions wherein intrinsic kinetics are measured in the absence of diffusion limitations. Spectroscopic techniques able to selectivity analyse interfaces, such as surface enhanced infrared absorption reaction spectroscopy will become increasingly valuable tools for understanding surface–adsorbate interaction,[162] and are best complemented by techniques such as XAS and XPS that interrogate the catalyst electronic and geometric structure.

Improved temporal resolution, particularly through the wider exploitation of pump–probe techniques,[163] into the pico- and femtosecond domains will expand our knowledge of elementary reaction steps in surface catalysis. Conversely, better approaches to undertaking stability testing to mimic industrial processes over days, weeks and even years, will better elucidate on-stream deactivation (and reactivation) mechanisms, but require new access routes to synchrotrons and related national facilities to enable acquisition of extended data-sets.[164] Closer alignment of *operando* conditions with those in used in industry is also necessary to enable better translation of laboratory findings to the 'real-world'; this is contingent on the design and commercial availability of reaction cells able to operate at elevated pressures >10 MPa (*e.g.* esterification and Diels–Alder[165]) and temperature >400 °C and with improved chemical tolerance to corrosive environments. Spatial resolution is another critical consideration, with spectral acquisition at the sub-micron scale by *e.g.* photoemission electron microscopy[166] enabling mapping of active site distributions, catalyst restructuring and concentration gradients at the solid–liquid interface, and at the cm to metre scale allowing chemical mapping of *e.g.* active site leaching and chemical speciation by XAS analysis across a reactor bed.[122]

The application of modulation excitation methods, in which one or more reaction parameters (such as temperature, reactant composition, pressure or voltage) are switched between different states, will provide unique insight into the nature of reactive intermediates in solid–liquid catalysis. Such studies have proven valuable for gas-phase systems,[167] and furthermore recent modelling[168,169] and experiments[170] have demonstrated that careful tuning of the modulation frequency can result in catalytic resonance offering the tantalising possibility of overcoming the Sabatier principle for static reactions, thereby unlocking rate enhancements of 10–10 000× for reactions such as formic acid electrooxidation. Inducing rapid switching of temperature, pressure and concentration will prove difficult for conventional liquid phase reactors, due to slow heat/mass transfer compared to gas phase catalysis, however the use of microfluidic reactors, and light or electrical[170] excitation for catalytic state-switching are promising solutions. Kinetic studies of rapid chemical transformations employing multidimensional spectroscopies will also generate vast datasets, requiring high capacity data compression/transfer/storage, and automated data processing and mining algorithms in conjunction with modelling/simulations (Machine Learning approaches[171,172]) to extract key descriptors for the development of next-generation catalysts.[173] *Operando* methodologies facilitate online analysis of catalytic processes and rapid feedback to optimise productivity, but require ultrafast data transfer and real-time data analysis. Advances in reactor design will aid the integration of *in situ* and *operando* spectroscopies, notably through advanced manufacturing techniques such as additive (3D) printing to fabricate novel reactor configurations with improved heat/mass transport and optical interfacing.[174] High throughput 3D printing directed by computational fluid dynamic modelling will permit the rapid evaluation of diverse reactor configurations that ensure spectroscopic measurements are acquired under real-world conditions.

Conflicts of interest

There are no conflicts to declare.

Acknowledgements

L. N. has received funding from the European Union's Horizon 2020 research and innovation programme under the Marie Skłodowska-Curie grant agreement No. 837794. The UK Catalysis Hub is kindly thanked for resources and support provided *via* membership of the UK Catalysis Hub Consortium and funded by EPSRC (portfolio grants EP/K014706/1, EP/K014668/1, EP/K014854/1, EP/K014714/1 and EP/I019693/1).

Notes and references

1 B. M. Weckhuysen, *Chem. Soc. Rev.*, 2010, **39**, 4557–4559.
2 U. Bentrup, *Chem. Soc. Rev.*, 2010, **39**, 4718–4730.
3 A. M. Beale, S. D. Jacques and B. M. Weckhuysen, *Chem. Soc. Rev.*, 2010, **39**, 4656–4672.
4 J. M. Andanson and A. Baiker, *Chem. Soc. Rev.*, 2010, **39**, 4571–4584.
5 S.-M. Xia, K.-H. Chen, H.-C. Fu and L.-N. He, *Front. Chem.*, 2018, **6**, 462.
6 A. R. Hind, S. K. Bhargava and A. McKinnon, *Adv. Colloid Interface Sci.*, 2001, **93**, 91–114.
7 R. A. Sheldon and R. S. Downing, *Appl. Catal., A*, 1999, **189**, 163–183.
8 K. J. Carpenter, *Chem. Eng. Sci.*, 2001, **56**, 305–322.
9 J. D. Grunwaldt and A. Baiker, *Phys. Chem. Chem. Phys.*, 2005, **7**, 3526–3539.
10 S. Gopalakrishnan, D. F. Liu, H. C. Allen, M. Kuo and M. J. Shultz, *Chem. Rev.*, 2006, **106**, 1155–1175.
11 T. Burgi, *Chimia*, 2003, **57**, 623–627.
12 B. L. Mojet, S. D. Ebbesen and L. Lefferts, *Chem. Soc. Rev.*, 2010, **39**, 4643–4655.

13 I. Ortiz-Hernandez, D. J. Owens, M. R. Strunk and C. T. Williams, *Langmuir*, 2006, **22**, 2629–2639.

14 T. Burgi and A. Baiker, *Adv. Catal.*, 2006, **50**, 227–283.

15 D. Ferri and A. Baiker, *Top. Catal.*, 2009, **52**, 1323–1333.

16 I. Ortiz-Hernandez and C. T. Williams, *Langmuir*, 2003, **19**, 2956–2962.

17 T. Burgi and A. Baiker, *J. Phys. Chem. B*, 2002, **106**, 10649–10658.

18 A. Urakawa, T. Bürgi and A. Baiker, *Chem. Eng. Sci.*, 2008, **63**, 4902–4909.

19 M. W. Urban, *J. Adhes. Sci. Technol.*, 1993, **7**, 1–47.

20 J. Yarwood, *Anal. Proc.*, 1993, **30**, 13–18.

21 L. J. Fina and G. Chen, *Vib. Spectrosc.*, 1991, **1**, 353–361.

22 J. Zakzeski, R. J. H. Grisel, A. T. Smit and B. M. Weckhuysen, *ChemSusChem*, 2012, **5**, 430–437.

23 A. L. Denning, H. Dang, Z. M. Liu, K. M. Nicholas and F. C. Jentoft, *ChemCatChem*, 2013, **5**, 3567–3570.

24 A. Wawrzetz, B. Peng, A. Hrabar, A. Jentys, A. A. Lemonidou and J. A. Lercher, *J. Catal.*, 2010, **269**, 411–420.

25 R. He, R. R. Davda and J. A. Dumesic, *J. Phys. Chem. B*, 2005, **109**, 2810–2820.

26 K. Koichumanova, A. K. K. Vikla, D. J. M. de Vlieger, K. Seshan, B. L. Mojet and L. Lefferts, *ChemSusChem*, 2013, **6**, 1717–1723.

27 J. R. Copeland, G. S. Foo, L. A. Harrison and C. Sievers, *Catal. Today*, 2013, **205**, 49–59.

28 S. D. Ebbesen, B. L. Mojet and L. Lefferts, *Langmuir*, 2006, **22**, 1079–1085.

29 S. D. Ebbesen, B. L. Mojet and L. Lefferts, *J. Catal.*, 2007, **246**, 66–73.

30 C. Keresszegi, D. Ferri, T. Mallat and A. Baiker, *J. Phys. Chem. B*, 2005, **109**, 958–967.

31 D. Ferri, T. Burgi and A. Baiker, *Phys. Chem. Chem. Phys.*, 2002, **4**, 2667–2672.

32 J. Y. Wang, H. X. Zhang, K. Jiang and W. B. Cai, *J. Am. Chem. Soc.*, 2011, **133**, 14876–14879.

33 A. Aguirre, P. A. Kler, C. L. A. Berli and S. E. Collins, *Chem. Eng. J.*, 2014, **243**, 197–206.

34 H. Knozinger and G. Mestl, *Top. Catal.*, 1999, **8**, 45–55.

35 I. E. Wachs and C. A. Roberts, *Chem. Soc. Rev.*, 2010, **39**, 5002–5017.

36 P. C. Stair, *Advances in Catalysis*, 2007, vol. 51, pp. 75–98.

37 S. Q. Jin, Z. C. Feng, F. T. Fan and C. Li, *Catal. Lett.*, 2015, **145**, 468–481.

38 S. Kim, L. Piao, D. Han, B. J. Kim and T. D. Chung, *Adv. Mater.*, 2013, **25**, 2056–2061.

39 L. Opilik, T. Schmid and R. Zenobi, *Annu. Rev. Anal. Chem.*, 2013, **6**, 379–398.

40 F. T. Fan, Z. C. Feng and C. Li, *Acc. Chem. Res.*, 2010, **43**, 378–387.

41 T. Kim, R. S. Assary, H. Kim, C. L. Marshall, D. J. Gosztola, L. A. Curtiss and P. C. Stair, *Catal. Today*, 2013, **205**, 60–66.

42 D. L. Jeanmaire and R. P. Van Duyne, *J. Electroanal. Chem. Interfacial Electrochem.*, 1977, **84**, 1–20.

43 H. Y. H. Chan, C. T. Williams, M. J. Weaver and C. G. Takoudis, *J. Catal.*, 1998, **174**, 191–200.

44 M. G. Albrecht and J. A. Creighton, *J. Am. Chem. Soc.*, 1977, **99**, 5215–5217.

45 K. N. Heck, B. G. Janesko, G. E. Scuseria, N. J. Halas and M. S. Wong, *ACS Catal.*, 2013, **3**, 2430–2435.

46 J. F. Li, Y. F. Huang, Y. Ding, Z. L. Yang, S. B. Li, X. S. Zhou, F. R. Fan, W. Zhang, Z. Y. Zhou, D. Y. Wu, B. Ren, Z. L. Wang and Z. Q. Tian, *Nature*, 2010, **464**, 392–395.

47 H. Zhang, S. Duan, P. M. Radjenovic, Z. Q. Tian and J. F. Li, *Acc. Chem. Res.*, 2020, **53**, 729–739.

48 Y. H. Wang, J. Wei, P. Radjenovic, Z. Q. Tian and J. F. Li, *Anal. Chem.*, 2019, **91**, 1675–1685.

49 J.-C. Dong, X.-G. Zhang, V. Briega-Martos, X. Jin, J. Yang, S. Chen, Z.-L. Yang, D.-Y. Wu, J. M. Feliu, C. T. Williams, Z.-Q. Tian and J.-F. Li, *Nat. Energy*, 2019, **4**, 60–67.

50 T. Deckert-Gaudig, A. Taguchi, S. Kawata and V. Deckert, *Chem. Soc. Rev.*, 2017, **46**, 4077–4110.

51 P. Verma, *Chem. Rev.*, 2017, **117**, 6447–6466.

52 A. Hartschuh, *Angew. Chem., Int. Ed.*, 2008, **47**, 8178–8191.

53 N. Kumar, W. T. Su, M. Vesely, B. M. Weckhuysen, A. J. Pollard and A. J. Wain, *Nanoscale*, 2018, **10**, 1815–1824.

54 N. Kumar, C. S. Wondergem, A. J. Wain and B. M. Weckhuysen, *J. Phys. Chem. Lett.*, 2019, **10**, 1669–1675.

55 S. Jiang, Z. Chen, X. Chen, D. Nguyen, M. Mattei, G. Goubert and R. P. Van Duyne, *J. Phys. Chem. C*, 2019, **123**, 9852–9859.

56 D. C. Koningsberger, *X-ray absorption: principles, applications, techniques of EXAFS, SEXAFS, and XANES*, John Wiley and Sons, United States, 1988.

57 A. F. Lee, V. Prabhakaran and K. Wilson, *Chem. Commun.*, 2010, **46**, 3827–3842.

58 G. A. Somorjai, S. K. Beaumont and S. Alayoglu, *Angew. Chem., Int. Ed.*, 2011, **50**, 10116–10129.

59 R. Toyoshima and H. Kondoh, *J. Phys. Condens. Matter*, 2015, **27**, 15.

60 H. L. Han, G. Melaet, S. Alayoglu and G. A. Somorjai, *ChemCatChem*, 2015, **7**, 3625–3638.

61 D. Bazin and L. Guczi, *Appl. Catal., A*, 2001, **213**, 147–162.

62 J. W. Smith and R. J. Saykally, *Chem. Rev.*, 2017, **117**, 13909–13934.

63 D. H. Bilderback, P. Elleaume and E. Weckert, *J. Phys. B: At., Mol. Opt. Phys.*, 2005, **38**, S773–S797.

64 G. T. Seidler, D. R. Mortensen, A. J. Remesnik, J. I. Pacold, N. A. Ball, N. Barry, M. Styczinski and O. R. Hoidn, *Rev. Sci. Instrum.*, 2014, **85**, 12.

65 E. P. Jahrman, W. M. Holden, A. S. Ditter, D. R. Mortensen, G. T. Seidler, T. T. Fister, S. A. Kozimor, L. F. J. Piper, J. Rana, N. C. Hyatt and M. C. Stennett, *Rev. Sci. Instrum.*, 2019, **90**, 15.

66 M. W. Tew, M. Nachtegaal, M. Janousch, T. Huthwelker and J. A. van Bokhoven, *Phys. Chem. Chem. Phys.*, 2012, **14**, 5761–5768.

67 A. L. Bugaev, A. A. Guda, A. Lazzarini, K. A. Lomachenko, E. Groppo, R. Pellegrini, A. Piovano, H. Emerich, A. V. Soldatov, L. A. Bugaev, V. P. Dmitriev, J. A. van Bokhoven and C. Lamberti, *Catal. Today*, 2017, **283**, 119–126.

68 V. M. Gonzalez-delaCruz, R. Pereniguez, F. Ternero, J. P. Holgado and A. Caballero, *J. Phys. Chem. C*, 2012, **116**, 2919–2926.

69 M. M. Gunter, T. Ressler, R. E. Jentoft and B. Bems, *J. Catal.*, 2001, **203**, 133–149.

70 N. E. Tsakoumis, A. Voronov, M. Ronning, W. van Beek, O. Borg, E. Rytter and A. Holmen, *J. Catal.*, 2012, **291**, 138–148.

71 M. Bron, D. Teschner, A. Knop-Gericke, A. Scheybal, B. Steinhauer, M. Havecker, R. Fodisch, D. Honicke, R. Schlogl and P. Claus, *Catal. Commun.*, 2005, **6**, 371–374.

72 H. J. Wei, C. Gomez, J. J. Liu, N. Guo, T. P. Wu, R. Lobo-Lapidus, C. L. Marshall, J. T. Miller and R. J. Meyer, *J. Catal.*, 2013, **298**, 18–26.

73 M. A. Newton, D. G. Burnaby, A. J. Dent, S. Diaz-Moreno, J. Evans, S. G. Fiddy, T. Neisius and S. Turin, *J. Phys. Chem. B*, 2002, **106**, 4214–4222.

74 M. A. Newton, C. Belver-Coldeira, A. Martinez-Arias and M. Fernandez-Garcia, *Nat. Mater.*, 2007, **6**, 528–532.

75 D. Ferri, M. S. Kumar, R. Wirz, A. Eyssler, O. Korsak, P. Hug, A. Weidenkaff and M. A. Newton, *Phys. Chem. Chem. Phys.*, 2010, **12**, 5634–5646.

76 M. A. Newton, M. Di Michiel, A. Kubacka and M. Fernández-García, *J. Am. Chem. Soc.*, 2010, **132**, 4540–4541.

77 S. T. Korhonen, A. M. Beale, M. A. Newton and B. M. Weckhuysen, *J. Phys. Chem. C*, 2011, **115**, 885–896.

78 A. F. Lee, C. V. Ellis, J. N. Naughton, M. A. Newton, C. M. A. Parlett and K. Wilson, *J. Am. Chem. Soc.*, 2011, **133**, 5724–5727.

79 A. F. Lee and K. Wilson, *Green Chem.*, 2004, **6**, 37–42.

80 C. M. A. Parlett, L. J. Durndell, A. Machado, G. Cibin, D. W. Bruce, N. S. Hondow, K. Wilson and A. F. Lee, *Catal. Today*, 2014, **229**, 46–55.

81 M. Makosch, C. Kartusch, J. Sa, R. B. Duarte, J. A. van Bokhoven, K. Kvashnina, P. Glatzel, D. L. A. Fernandes, M. Nachtegaal, E. Kleymenov, J. Szlachetko, B. Neuhold and K. Hungerbuhler, *Phys. Chem. Chem. Phys.*, 2012, **14**, 2164–2170.

82 S. Kanungo, L. van Haandel, E. J. M. Hensen, J. C. Schouten and M. F. N. d'Angelo, *J. Catal.*, 2019, **370**, 200–209.

83 R. S. Weatherup, *Top. Catal.*, 2018, **61**, 2085–2102.

84 G. Pacchioni, *Nat. Rev. Phys.*, 2019, **1**, 100–101.

85 E. de Smit, I. Swart, J. F. Creemer, G. H. Hoveling, M. K. Gilles, T. Tyliszczak, P. J. Kooyman, H. W. Zandbergen, C. Morin, B. M. Weckhuysen and F. M. F. de Groot, *Nature*, 2008, **456**, 222–225.

86 J. D. Grunwaldt, C. Keresszegi, T. Mallat and A. Baiker, *J. Catal.*, 2003, **213**, 291–295.

87 J. D. Grunwaldt, M. Caravati and A. Baiker, *J. Phys. Chem. B*, 2006, **110**, 25586–25589.

88 J.-D. Grunwaldt, M. Caravati and A. Baiker, *J. Phys. Chem. B*, 2006, **110**, 9916–9922.

89 A. F. Lee, *Abstr. Pap. Am. Chem. Soc.*, 2001, vol. 221, p. 187-COLL.

90 A. F. Lee, J. J. Gee and H. J. Theyers, *Green Chem.*, 2000, **2**, 279–282.

91 A. F. Lee, Z. Chang, P. Ellis, S. F. J. Hackett and K. Wilson, *J. Phys. Chem. C*, 2007, **111**, 18844–18847.

92 A. F. Lee, J. N. Naughton, Z. Liu and K. Wilson, *ACS Catal.*, 2012, **2**, 2235–2241.

93 C. V. Gaskell, C. M. A. Parlett, M. A. Newton, K. Wilson and A. F. Lee, *ACS Catal.*, 2012, **2**, 2242–2246.

94 C. M. A. Parlett, C. V. Gaskell, J. N. Naughton, M. A. Newton, K. Wilson and A. F. Lee, *Catal. Today*, 2013, **205**, 76–85.

95 S. F. J. Hackett, R. M. Brydson, M. H. Gass, I. Harvey, A. D. Newman, K. Wilson and A. F. Lee, *Angew. Chem., Int. Ed.*, 2007, **46**, 8593–8596.

96 H. Chen, S. He, M. Xu, M. Wei, D. G. Eyans and X. Duan, *ACS Catal.*, 2017, **7**, 2735–2743.

97 T. Balcha, J. R. Strobl, C. Fowler, P. Dash and R. W. J. Scott, *ACS Catal.*, 2011, **1**, 425–436.

98 A. Maclennan, A. Banerjee, Y. F. Hu, J. T. Miller and R. W. J. Scott, *ACS Catal.*, 2013, **3**, 1411–1419.

99 R. Y. Zheng, M. D. Porosoff, J. L. Weiner, S. L. Lu, Y. X. Zhu and J. G. G. Chen, *Appl. Catal., A*, 2012, **419**, 126–132.

100 K. Taniya, H. Jinno, M. Kishida, Y. Ichihashi and S. Nishiyama, *J. Catal.*, 2012, **288**, 84–91.

101 S. Nishimura, N. Ikeda and K. Ebitani, *Catal. Today*, 2014, **232**, 89–98.

102 K. Shimizu, Y. Miyamoto, T. Kawasaki, T. Tanji, Y. Tai and A. Satsuma, *J. Phys. Chem. C*, 2009, **113**, 17803–17810.

103 N. M. Bertero, A. F. Trasarti, B. Moraweck, A. Borgna and A. J. Marchi, *Appl. Catal., A*, 2009, **358**, 32–41.

104 U. Hartfelder, C. Kartusch, M. Makosch, M. Rovezzi, J. Sa and J. A. van Bokhoven, *Catal. Sci. Technol.*, 2013, **3**, 454–461.

105 H. G. Manyar, R. Morgan, K. Morgan, B. Yang, P. Hu, J. Szlachetko, J. Sa and C. Hardacre, *Catal. Sci. Technol.*, 2013, **3**, 1497–1500.

106 S. Schuster, E. Klemm and M. Bauer, *Chem. – Eur. J.*, 2012, **18**, 15831–15837.

107 V. F. Kispersky, A. J. Kropf, F. H. Ribeiro and J. T. Miller, *Phys. Chem. Chem. Phys.*, 2012, **14**, 2229–2238.

108 B. J. O'Neill, J. T. Miller, P. J. Dietrich, F. G. Sollberger, F. H. Ribeiro and J. A. Dumesic, *ChemCatChem*, 2014, **6**, 2493–2496.

109 R. J. Lewis and G. J. Hutchings, *ChemCatChem*, 2019, **11**, 298–308.

110 P. Centomo, C. Meneghini and M. Zecca, *Rev. Sci. Instrum.*, 2013, **84**, 5.

111 P. Centomo, C. Meneghini, S. Sterchele, A. Trapananti, G. Aquilanti and M. Zecca, *Catal. Today*, 2015, **248**, 138–141.

112 L. Ouyang, P. F. Tian, G. J. Da, X. C. Xu, C. Ao, T. Y. Chen, R. Si, J. Xu and Y. F. Han, *J. Catal.*, 2015, **321**, 70–80.

113 M. Selinsek, B. J. Deschner, D. E. Doronkin, T. L. Sheppard, J. D. Grunwaldt and R. Dittmeyer, *ACS Catal.*, 2018, **8**, 2546–2557.

114 A. M. Karim, C. Howard, B. Roberts, L. Kovarik, L. Zhang, D. L. King and Y. Wang, *ACS Catal.*, 2012, **2**, 2387–2394.

115 Z. H. Wei, A. Karim, Y. Li and Y. Wang, *ACS Catal.*, 2015, **5**, 7312–7320.

116 Z. H. Wei, A. M. Karim, Y. Li, D. L. King and Y. Wang, *J. Catal.*, 2015, **322**, 49–59.

117 P. J. Dietrich, R. J. Lobo-Lapidus, T. P. Wu, A. Sumer, M. C. Akatay, B. R. Fingland, N. Guo, J. A. Dumesic, C. L. Marshall, E. Stach, J. Jellinek, W. N. Delgass, F. H. Ribeiro and J. T. Miller, *Top. Catal.*, 2012, **55**, 53–69.

118 P. J. Ellis, I. J. S. Fairlamb, S. F. J. Hackett, K. Wilson and A. F. Lee, *Angew. Chem., Int. Ed.*, 2010, **49**, 1820–1824.

119 A. F. Lee, P. J. Ellis, I. J. S. Fairlamb and K. Wilson, *Dalton Trans.*, 2010, **39**, 10473–10482.

120 L. A. Adrio, B. N. Nguyen, G. Guilera, A. G. Livingston and K. K. Hii, *Catal. Sci. Technol.*, 2012, **2**, 316–323.

121 J. B. Brazier, B. N. Nguyen, L. A. Adrio, E. M. Barreiro, W. P. Leong, M. A. Newton, S. J. A. Figueroa, K. Hellgardt and K. K. M. Hii, *Catal. Today*, 2014, **229**, 95–103.

122 M. A. Newton, J. B. Brazier, E. M. Barreiro, S. Parry, H. Emmerich, L. A. Adrio, C. J. Mulligan, K. Hellgardt and K. K. Hii, *Green Chem.*, 2016, **18**, 406–411.

123 M. A. Newton, J. B. Brazier, E. M. Barreiro, H. Emerich, L. A. Adrio, C. J. Mulligan, K. Hellgardt and K. K. Hii, *Catal. Sci. Technol.*, 2016, **6**, 8525–8531.

124 S. Reimann, J. D. Grunwaldt, T. Mallat and A. Baiker, *Chem. – Eur. J.*, 2010, **16**, 9658–9668.

125 S. Reimann, J. Stotzel, R. Frahm, W. Kleist, J. D. Grunwaldt and A. Baiker, *J. Am. Chem. Soc.*, 2011, **133**, 3921–3930.

126 N. Yuan, V. Pascanu, Z. H. Huang, A. Valiente, N. Heidenreich, S. Leubner, A. K. Inge, J. Gaar, N. Stock, I. Persson, B. Martin-Matute and X. D. Zou, *J. Am. Chem. Soc.*, 2018, **140**, 8206–8217.

127 M. P. Seah, *Vacuum*, 1984, **34**, 463–478.

128 A. M. Venezia, *Catal. Today*, 2003, **77**, 359–370.

129 K. Siegbahn, C. Nordling, G. Johansson, J. Hedman, P. F. Heden, K. Hamrin, U. Gelius, T. Bergmark, L. O. Werme, R. Manne and Y. Baer, *ESCA Applied to Free Molecules*, North-Holland, 1969.

130 D. F. Ogletree, H. Bluhm, G. Lebedev, C. S. Fadley, Z. Hussain and M. Salmeron, *Rev. Sci. Instrum.*, 2002, **73**, 3872–3877.

131 M. Salmeron and R. Schlögl, *Surf. Sci. Rep.*, 2008, **63**, 169–199.

132 H. Bluhm, *J. Electron Spectrosc. Relat. Phenom.*, 2010, **177**, 71–84.

133 D. Starr, Z. Liu, M. Hävecker, A. Knop-Gericke and H. Bluhm, *Chem. Soc. Rev.*, 2013, **42**, 5833–5857.

134 A. Knop-Gericke, V. Pfeifer, J.-J. Velasco-Velez, T. Jones, R. Arrigo, M. Hävecker and R. Schlögl, *J. Electron Spectrosc. Relat. Phenom.*, 2017, **221**, 10–17.

135 O. Karslıoğlu, S. Nemšák, I. Zegkinoglou, A. Shavorskiy, M. Hartl, F. Salmassi, E. Gullikson, M. Ng, C. Rameshan and B. Rude, *Faraday Discuss.*, 2015, **180**, 35–53.

136 P. Kolb, D. Rath, R. Wille and W. Hansen, *Berichte der Bunsengesellschaft für physikalische Chemie*, 1983, **87**, 1108–1113.

137 K. Roy, L. Artiglia and J. A. van Bokhoven, *ChemCatChem*, 2018, **10**, 666–682.

138 M. Favaro, F. F. Abdi, E. J. Crumlin, Z. Liu, R. van de Krol and D. E. Starr, *Surfaces*, 2019, **2**, 78–99.

139 S. Axnanda, E. J. Crumlin, B. Mao, S. Rani, R. Chang, P. G. Karlsson, M. O. Edwards, M. Lundqvist, R. Moberg and P. Ross, *Sci. Rep.*, 2015, **5**, 9788.

140 K. Arima, P. Jiang, X. Deng, H. Bluhm and M. Salmeron, *J. Phys. Chem. C*, 2010, **114**, 14900–14906.

141 S. Nemšák, A. Shavorskiy, O. Karslioglu, I. Zegkinoglou, A. Rattanachata, C. S. Conlon, A. Keqi, P. K. Greene, E. C. Burks and F. Salmassi, *Nat. Commun.*, 2014, **5**, 1–7.

142 Y. Takagi, H. Wang, Y. Uemura, T. Nakamura, L. Yu, O. Sekizawa, T. Uruga, M. Tada, G. Samjeské and Y. Iwasawa, *Phys. Chem. Chem. Phys.*, 2017, **19**, 6013–6021.

143 H. Ali-Löytty, M. Hannula, M. Valden, A. Eilert, H. Ogasawara and A. Nilsson, *J. Phys. Chem. C*, 2019, **123**, 25128–25134.

144 M. Faubel, B. Steiner and J. P. Toennies, *J. Chem. Phys.*, 1997, **106**, 9013–9031.

145 M. A. Brown, N. Duyckaerts, A. B. Redondo, I. Jordan, F. Nolting, A. Kleibert, M. Ammann, H. J. Wörner, J. A. Van Bokhoven and Z. Abbas, *Langmuir*, 2013, **29**, 5023–5029.

146 R. Arrigo, M. Hävecker, M. E. Schuster, C. Ranjan, E. Stotz, A. Knop-Gericke and R. Schlögl, *Angew. Chem., Int. Ed.*, 2013, **52**, 11660–11664.

147 V. Pfeifer, T. E. Jones, J. J. V. Vélez, R. Arrigo, S. Piccinin, M. Hävecker, A. Knop-Gericke and R. Schlögl, *Chem. Sci.*, 2017, **8**, 2143–2149.

148 A. Kolmakov, E. Strelcov, H. Guo, A. Yulaev, B. Hoskins, G. Holland, S. Nemsak, C. M. Schneider, J. Wang, N. Appathurai, S. Urquhart, S. Gunther, L. Gregoratti, M. Amati and M. Kiskinova, *Microsc. Microanal.*, 2018, **24**, 64–67.

149 R. S. Weatherup, B. Eren, Y. Hao, H. Bluhm and M. B. Salmeron, *J. Phys. Chem. Lett.*, 2016, **7**, 1622–1627.

150 R. Mom, L. Frevel, J.-J. S. Velasco-Vélez, M. Plodinec, A. Knop-Gericke and R. Schlögl, *J. Am. Chem. Soc.*, 2019, **141**, 6537–6544.

151 J. J. Velasco-Velez, V. Pfeifer, M. Hävecker, R. S. Weatherup, R. Arrigo, C. H. Chuang, E. Stotz, G. Weinberg, M. Salmeron and R. Schlögl, *Angew. Chem., Int. Ed.*, 2015, **54**, 14554–14558.

152 M. Al-Hada, M. Amati, H. Sezen, L. Cozzarini and L. Gregoratti, *Catal. Lett.*, 2018, **148**, 2247–2255.

153 S. Nappini, A. Matruglio, D. Naumenko, S. Dal Zilio, F. Bondino, M. Lazzarino and E. Magnano, *Nanoscale*, 2017, **9**, 4456–4466.

154 T. Burgi, *J. Catal.*, 2005, **229**, 55–63.

155 C. P. Stemmet, J. C. Schouten and T. A. Nijhuis, *Chem. Eng. Sci.*, 2010, **65**, 267–272.

156 C. D. Bain, *J. Chem. Soc., Faraday Trans.*, 1995, **91**, 1281–1296.

157 A. J. Hopkins, C. L. McFearin and G. L. Richmond, *Curr. Opin. Solid State Mater. Sci.*, 2005, **9**, 19–27.

158 S. B. Waldrup and C. T. Williams, *Catal. Commun.*, 2007, **8**, 1373–1376.

159 Z. Lu, A. Karakoti, L. Velarde, W. N. Wang, P. Yang, S. Thevuthasan and H. F. Wang, *J. Phys. Chem. C*, 2013, **117**, 24329–24338.

160 J. F. Gomes, K. Bergamaski, M. F. S. Pinto and P. B. Miranda, *J. Catal.*, 2013, **302**, 67–82.

161 R. Schlögl, in *Basic Principles in Applied Catalysis*, ed. M. Baerns, Springer Berlin Heidelberg, Berlin, Heidelberg, 2004, pp. 321–360, DOI: 10.1007/978-3-662-05981-4_9.

162 N. S. Gould and B. J. Xu, *Chem. Sci.*, 2018, **9**, 281–287.

163 J. Bredenbeck, A. Ghosh, H. K. Nienhuys and M. Bonn, *Acc. Chem. Res.*, 2009, **42**, 1332–1342.

164 C. Hammond, *Green Chem.*, 2017, **19**, 2711–2728.

165 A. Adeyemi, J. Bergman, J. Brånalt, J. Sävmarker and M. Larhed, *Org. Process Res. Dev.*, 2017, **21**, 947–955.

166 H. Guo, E. Strelcov, A. Yulaev, J. Wang, N. Appathurai, S. Urquhart, J. Vinson, S. Sahu, M. Zwolak and A. Kolmakov, *Nano Lett.*, 2017, **17**, 1034–1041.

167 M. A. Newton, *Catalysts*, 2017, **7**, 58.

168 M. A. Ardagh, T. Birol, Q. Zhang, O. A. Abdelrahman and P. J. Dauenhauer, *Catal. Sci. Technol.*, 2019, **9**, 5058–5076.

169 M. A. Ardagh, O. A. Abdelrahman and P. J. Dauenhauer, *ACS Catal.*, 2019, **9**, 6929–6937.

170 G. Joshua, A. Matthew, S. Manish, B. Sean, D. Paul and A. Omar, *Resonance-Promoted Formic Acid Oxidation via Dynamic Electrocatalytic Modulation*, 2020.

171 J. R. Kitchin, *Nat. Catal.*, 2018, **1**, 230–232.

172 B. R. Goldsmith, J. Esterhuizen, J.-X. Liu, C. J. Bartel and C. Sutton, *AIChE J.*, 2018, **64**, 2311–2323.

173 M. Basham, J. Filik, M. T. Wharmby, P. C. Y. Chang, B. El Kassaby, M. Gerring, J. Aishima, K. Levik, B. C. A. Pulford, I. Sikharulidze, D. Sneddon, M. Webber, S. S. Dhesi, F. Maccherozzi, O. Svensson, S. Brockhauser, G. Naray and A. W. Ashton, *J. Synchrotron Radiat.*, 2015, **22**, 853–858.

174 E. Achilli, A. Minguzzi, A. Visibile, C. Locatelli, A. Vertova, A. Naldoni, S. Rondinini, F. Auricchio, S. Marconi, M. Fracchia and P. Ghigna, *J. Synchrotron Radiat.*, 2016, **23**, 622–628.